

## 9.0 GLOBAL SFMT POSTTEST ANALYSIS

### 9.1 The Structural Failure Mode Test and SFMT Analysis Objectives

The work described in this report provided detailed documentation of comparisons of the pretest analyses to the test measurements, made adjustments to analytical models for measured material properties or material conditions, and explained and quantified behaviors and failure modes observed in the test. The overall goal of documenting analysis improvements and lessons learned, however, was limited to the context of what was learned from the LST; namely, that associated with PCCV pressure response out to global hoop strains was only about 0.5%, and liner tearing failure modes may have occurred prematurely due to welding irregularities. To obtain further information from the PCCV model, a SFMT was conducted in November 2001. In this test, the existing steel liner was relined with a heavy plastic liner and the testing medium was changed to hydrostatic, driven by nitrogen, which was pumped into a much smaller gas volume, as shown in Figure 9-1.

The SFMT resulted in a completely different failure mode: a catastrophic burst of the vessel. Additional measurement data was obtained much further into the nonlinear response range of the structure than in the LST, i.e., up to global hoop strains of nearly 2%. The rapid failure mode that followed was also captured on video. Some still photos from this video are shown in Figures 9-2 and 9-3, and the rupture pattern that occurred is shown in Figure 9-4. SNL provided some posttest observations of the SFMT.

- The maximum pressure reached (average pressure by volume) was ~1.424 MPa, or ~3.6 Pd.
- The water level inside the model visibly dropped slightly just before the rupture of the PCCV.
- Four to six tendons failed in the final minute before the vessel ruptured, and nearly all cylinder hoop tendons were ruptured by the end of the test.
- Rupture initiated at approximately midheight of the cylinder near azimuth 6 degrees, then radiated vertically in both directions; a subsequent rupture line radiated circumferentially approximately 1.5 m above the top of the basemat.
- The vessel “telescoped” over the stem of the cylinder wall and came to rest on the instrumentation frame.
- Approximately 12 tendon segments were completely ejected from the model (all remained within test site boundaries).
- Hoop tendons and rebar at the rupture line exhibited significant necking, indicating that rupture was ductile in nature.
- The model displaced 3 inches horizontally and tipped in the opposite direction from the rupture. This was likely caused by the momentum transfer that resulted from water jetting from the rupture zone.

In order to maximize the utility and lessons learned from the SFMT, analytical studies of this final test were undertaken. The additional studies consisted of two subtasks:

1. Comparing the measurements taken to existing analyses, and to new analyses which replicate the conditions of the SFMT, and
2. Conducting a new analysis using a simplified 3D model.

### 9.2 Posttest SFMT Global Model

The SFMT posttest analysis model is a fully 3D model of the entire containment cylinder, dome, and basemat, which focuses on capturing the global behavior versus pressure up to the tendon rupture observed in the SFMT. The containment was modeled with shell elements, which required a bonded tendon assumption for the post-tensioned tendons and was simpler to model than the pretest 3DCM model. The ABAQUS general-purpose finite element program Version 5.8-18, along with the ANACAP-U concrete and steel constitutive modeling program, was used for the SFMT analysis, just as for the other posttest work.

A layered shell model was developed that included the liner and concrete as separate layers; rebar subelements were used to model the reinforcement and tendons. The E/H and A/L penetrations of the PCCV were explicitly modeled, with emphasis on their associated perturbations in rebar and tendon patterns and increased wall thickness. The M/S and

F/W penetrations were not modeled explicitly, since these penetrations cause negligible perturbation of the tendon pattern. However, the additional reinforcement associated with these penetrations and the thickening of the liner was included. The model consisted of 4-node composite (layered) shell elements. The inner layer simulated the 1.6 mm thick steel liner and the outer layer was given properties consistent with the concrete wall, including the differing thickness of the wall at the buttress, springline, dome, and E/H and A/L penetration regions. Both the liner and concrete layers were each assigned three integration points through the thickness. The basemat was also modeled with composite shell elements and rebar subelements, but the tendon gallery was not explicitly modeled. The horizontal plane of nodes making up the basemat was located at the geometric centerline of the region, approximately 180 cm (70 inches) below the base of the containment wall. The nodes at the base of the cylinder wall were tied to corresponding nodes in the horizontal plane of the basemat with multipoint constraint equations. The bottom of the basemat was modeled with nonlinear spring elements with an average spring constant of 150.5 kips per square inch in compression; the tensile/uplift stiffness was very small. The finite element mesh is shown in Figure 9-5.

The reinforcement was modeled as subelements within the shell elements at the correct section depth. Figure 9-6 shows the inner and outer layers of vertical reinforcement in the cylinder and the dome regions. The two layers of hoop reinforcement are shown in Figure 9-7. The bonded post-tensioned tendons are also modeled as rebar subelements within the shell elements, as shown in Figure 9-8. The perturbation of the meridional and hoop tendons around the A/L is accurately simulated. In the local region of the E/H where the hoop tendons overlap through the thickness, they were combined in groups of two with the total properties of the pair located at the geometric centroid of the two tendons. The tendons were post-tensioned by applying an initial stress to the specific tendon subelements. To address the issue of tendon friction, which was studied in detail in the 3DCM analysis, two versions of tendon initial stress were analyzed: one with variable stress around the circumference, as a function of friction and setting losses, and the other uniform tendon prestress, set to the average value of tendon stress.

Figure 9-9 shows additional local reinforcement in the buttresses at 90 and 270 degrees and the ring hoops at the E/H and A/L openings.

Pressure load was applied to all interior model surfaces. At the E/H and A/L openings, the pressure load was increased on the first row of elements around the circumference to apply the same load at these regions that would develop due to pressure applied on the covering over these penetrations. The load sequence included a preloading step that pressurized the model to 3.2 Pd (1.257 MPa), approximately the pressurization achieved in the LST test, and then unloaded it. After the preloading, a hydrostatic water pressure load was applied to the interior surfaces equivalent to a head of approximately 14.8 m to simulate the PCCV filled with water to 1.3 m from the top of the dome. Additional pressure was then ramped up on the interior surfaces in addition to the hydrostatic loading.

### 9.3 Results and Comparisons

Displacement versus pressure histories at various locations are compared to the SFMT in Figures 9-10 through 9-15. The displacement data from the test is plotted along with posttest analysis data from the model with uniform average tendon stress, and from the analysis with variable tendon post-tensioning stresses. The displacements are plotted versus the total internal pressure, including the hydrostatic component. The average pressure is the gas pressure plus the hydrostatic pressure that exists near the midheight of the cylinder (i.e., at an elevation of approximately 5.0 m). Table 9-1 summarizes the figure number, gage location, azimuth, elevation, and displacement component used for these comparisons.

At azimuth 135 degrees, elevations 2.63 and 6.2 m, the pretest analysis results were also added to the plots.

Maximum principal strain contour plots for the analysis with tendon friction losses are shown in Figures 9-16 through 9-23. The series shows views from azimuth locations 0 and 90 degrees, and views from 180 and 270 degrees. The inside liner strains at a total pressure load of 1.28 MPa, approximately 3.25 Pd, are shown in Figures 9-16 and 9-17. At the same pressure, the outer concrete strains are shown in Figure 9-18 and 9-19. Figures 9-20 to 9-23 show the maximum liner and concrete strains, respectively, at a pressure load of 1.44 MPa, approximately 3.65 Pd. This is approximately equal to the maximum pressure achieved during the SFMT.

**Table 9-1. Gage Displacement Comparison**

Figure	Gage	Azimuth	Elevation	Displacement
9-10	R-Z4-05	135 degrees	2.63 m	Radial
9-11	R-D5-05	90 degrees	4.68 m	Radial
9-12	R-I5-05	240 degrees	4.68 m	Radial
9-13	R-Z6-05	135 degrees	6.20 m	Radial
9-14	R-L9-05	324 degrees	10.75 m	Radial
9-15	M-L9-05	324 degrees	10.75 m	Vertical

The plots in this section generally show a good correlation between the analysis and the PCCV SFMT response. The displacement behavior predicts the actual displacement well (to within a few percent over most of the pressure response range), and the strain contour plots indicate that failure is predicted between 0 degrees azimuth and 6 degrees azimuth, which agrees well with observations from the SFMT. The pretest axisymmetric analysis also agrees well with the SFMT response, at least for midheight of cylinder radial displacement. It is interesting to note the effects of running LST pressurization first. The LST pressure response of the vessel shows a little larger stiffness (slope of displacement versus pressure curve) than the SFMT reload. The tendon behavior plots indicate that for the baseline analysis, the first tendons rupture at elevation 5.5 m at a pressure load of 3.51 Pd (1.381 MPa).

To address the shear failure that occurred about 1.5 m from the basemat the element section forces were saved for a circumferential band of elements that straddled the 1.5 m elevation point.

#### 9.4 Tendon Rupture Analysis

In order to simulate and examine the sequence of events that likely occurred just before vessel failure, a “tendon rupture” analysis was run where the tendon failure criteria for rupture was adjusted to occur at 2% strain. (The non-tendon rupture analysis had tendon rupture set at 4% strain, which was the mean from tendon tests. The 2% is justified by the lower bounds of the tendon tests [8].) This was incorporated into the global shell model with the distributed friction losses. Figures 9-24 and 9-25 show outer concrete maximum principal strain contours at pressure loads of 3.47, 3.49, 3.51, and 3.53 Pd (1.365, 1.372, 1.381, and 1.388 Mpa, respectively). The first failure occurs near the 0 degrees azimuth. The adjacent elements span approximately 6 degrees at this region, so this could be considered to be a measure of the precision of the location prediction. Figures 9-26 and 9-27 show deformation plots of a circumferential band of elements at an elevation of 5.4 m and 6.5 m for each of the pressure loads shown in the previous strain contour plots. These plots also confirm the presence of a significant bulge predicted at pressures larger than 3.5 Pd.

A series of hoop tendon stress versus strain history plots are shown in Figures 9-28 through 9-34. These plots show the stress/strain status of individual tendons and demonstrate analytical prediction of tendons rupturing one at a time. Each plot shows the stress-strain response of hoop tendons at elevations 1.7, 2.6, 3.7, 4.7, 5.4, 6.5, 7.8, 8.6, 9.4, and 10.6 m above the basemat at the 0 degrees azimuth. The individual plots show a snapshot of the tendon behavior at pressure loads of 3.45 Pd (1.357 MPa) in Figure 9-28, and 3.47 Pd (1.365 MPa), 3.49 Pd (1.372 MPa), 3.51 Pd (1.381 MPa), 3.53 Pd (1.388 MPa), 3.57 Pd (1.403 MPa), and 3.65 Pd (1.435 MPa) in Figure 9-34. Hoop tendon strain profiles around the circumference at elevations of 5.8, 6.1, 6.3, 6.5, 6.8, and 7.1 m are shown in Figures 9-35 through 9-41. These plots are at the same load steps as the previous hoop tendon stress strain response plots. They show the variation of hoop strain around the circumference and show how maximum strain always occurs near 0 degrees azimuth. Note that the relatively sharp strain gradients evidenced in these figures may be artifacts of the bonded tendon assumption.

Figures 9-42 and 9-43 show the shear forces and stresses, respectively, around the circumference for design load pressure multiples of 3.05, 3.25, 3.45, and 3.65. It is clear that there are elevated shear stresses at the buttresses and between azimuths 20 to 50 degrees.

The progression of tendon stress-strain, Figures 9-28 through 9-34, is also summarized in Table 9-2.

**Table 9-2. Peak Strain in Hoop Tendons from SFMT Rupture Analysis at Multiples of Design Pressure**

Tendon Elev. (m)	3.45	3.47	3.49	3.51	3.53	3.57	3.65
1.7	.00771	.00775	.00780	.00784	.00789	.00812	.00977
2.6	.00886	.00898	.00914	.00930	.00951	.010343	.01547
3.7	.01121	.01176	.01238	.01313	.01411	.01807	.05976
4.7	.01346	.01420	.01506	.01621	.01836	.02451	.08797
5.4	.01702	.01807	.01928*	.02136	.03112	.06738	.12572
6.5	.01685	.01788	.01909	.02293	.03715	.06734	.12342
7.8	.01082	.01125	.01176	.01238	.01323	.01580	.04466
8.6	.01027	.01065	.01109	.01158	.01219	.01385	.02163
9.4	.00942	.00976	.01008	.01046	.01090	.01203	.01642
10.6	.00812	.00833	.00854	.00880	.00906	.00969	0.0117

\* Approaching first rupture (i.e., tendon rupture redefined to be  $\epsilon = 0.02$ )

The plots and table show that first rupture initiates at elev. 5.4 m,  $P = 3.49$  Pd, but then quickly spreads up to elev. 6.5 m by 3.51 Pd. By 3.57 Pd, rupture spreads down to 4.7 m, and by 3.65 Pd, it has spread to as low as elev. 3 m and as high as 8.6 m.

## 9.5 Conclusions of the SFMT Analysis

The SFMT posttest analysis has shown that good simulation of the PCCV global behavior up through and including tendon rupture failures is possible with a 3D shell model. Although the model is still very complex, the shell element simplification allowed model development and analysis in just a few months and reasonable run-time, i.e., a couple of hours rather than days on a modern workstation. The main limitations of the shell model are lack of local liner strain concentration prediction and lack of accuracy in the predictions of local wall-base-juncture behavior. Significant accuracy in global behavior prediction did not seem to be lost when a bonded tendon assumption was used, but some method of accounting for initial friction losses was still desirable.

It is clear from the video coverage of the test that the rupture occurred near cylinder midheight and near 6 degrees azimuth. The SFMT analysis model provides additional insight as to how this failure likely developed. Prior to  $P = 3$  Pd the 0 to 6 degrees azimuth location, elev. 5 m was behaving similarly to other azimuths away from penetrations. After 3.2 Pd, a few hot spots emerged around this elevation: a) edge of E/H wall embossment, b) edges of M/S penetration, and c) this  $\sim 0$  degree location. In each case, the cause of the hot spot appears to be the location's position relative to a stiffness discontinuity. In the case of the 0 degree location, the discontinuity is a step down in inner and outer hoop rebar area totaling 38% (step-down from alternating D19, D16 bars to a pattern of 1D16/3D13 bars). Then at 3.49 Pd, while the other locations also showed elevated strain, the wall and tendon strain at the 0 to 6 degree location was the highest, and a tendon ruptures. Once this occurs, the analysis shows the neighboring tendons rupturing and the deformations spread quickly at this azimuth. It is interesting to note that the analysis predicts the secondary tendon ruptures spread upward. Shortly after the first rupture at 5.4 m, analysis predicts the tendon ruptures to spread up through 6.5 m. From review of the test video, this appears to also agree with observations. By 3.65 Pd, the analysis shows rupture to have spread over a vertical line spanning up to 6 m. This also agrees with observations.

After wall rupture, a secondary event occurred in the SFMT; the through-wall failure around the circumference of the wall at about 1.5 m elevation. While it is difficult to say at what azimuth this failure initiated, it seems clear that this was a shear or combined shear/flexural failure of the wall. The plotting of analysis shear results (force and stress) in Figures 6-42 and 6-43 show that such failure may have initiated at the buttresses (evidenced by the high shear stresses predicted there) and then "unzipped." Upon reviewing the plans again, it can be noted that at elev. 1.60 m there is a step-down in vertical rebar from D19 to D16, which may have focused this shear failure plane. Moreover, at the buttresses, the outer vertical rebar step down occurs slightly lower: at 1.22 m there is a change from a total of 19D19 bars down to a total of 10D19 bars placed within the buttress. This may explain why the circumferential failure (see Figure 9-4) ran through the buttresses at a lower elevation than the rest of the wall. As a point of comparison, the shear failure threshold calculation performed in the pretest work [1] is compared to the demand (both pretest axisymmetric and posttest SFMT) in Figure 9-44. This figure shows that without the trigger of rupture of the vessel, the capacity (a modified compression

field theory calculation shown here as an average shear stress through the wall) exceeds the demand throughout the pressurization. But with the triggering event of a massive wall rupture, one of two mechanisms may have caused shear demand to exceed capacity.

1. Large deformation of the wall opening, creating large rotations near the base of the wall, would crush the outer concrete of the flexural section and thereby reduce the capacity (as would be predicted by modified compression field theory or other methods);
2. The water jet-induced momentum imbalance would cause added shear demand; using beam theory, this would create tangential shear at some azimuths that would be maximum at the buttresses; such shear acting in combination with the already high radial shear stresses could have increased shear stress demand enough to induce the shear failure.

Both of these potential mechanisms are illustrated in Figure 9-44.

The SFMT posttest analysis showed that reasonable simulation of the PCCV global behavior through and including tendon rupture was possible with a 3D shell model. The main limitations of the shell model were lack of local liner strain concentration prediction and lack of accuracy in the predictions of local wall-base-juncture behavior. However, significant accuracy in global behavior prediction was not lost when a bonded tendon assumption was used. Analysis considering initial tendon friction did provide slightly closer correlation to the test than analysis without considering initial friction losses. The SFMT model provided additional insight as to how the structural failure likely developed. Near the 0-6 degrees azimuth of the cylinder, there is a discontinuity of a step-down in inner and outer hoop rebar area of 38% (step-down from alternating D19, D16 bars to a pattern of 1D16/3D13 bars). Then at 3.49 Pd, the wall and tendon strain at the 0-6 degrees location is a little higher than all other azimuths, and a tendon rupture occurs. After this, the analysis shows neighboring tendons rupturing and the deformations spreading quickly along this azimuth. Shortly after the first rupture at 5.4 m elevation, the analysis predicted the tendon ruptures to spreading up through 6.5 m. From a review of the test video, this appears to agree with observations. By 3.65 Pd, the analysis shows rupture to have spread over a vertical line spanning about 6 m. This also agrees with observations. After wall rupture, a secondary event occurred in the SFMT: through-wall failure around the circumference of the wall at about 1.5 m elevation. While it is difficult to say at what azimuth this failure initiated, it seems clear that this was a shear or combined shear/flexural failure of the wall. The shell model provided only limited information for studying this phenomena, but it did provide the radial shear demands at all azimuths, which indicated that shear demands were highest at the buttresses. As with the vertical failure line in the cylinder, the circumferential failure line near the bottom of the cylinder appears to have occurred at or near a step-down in reinforcement.

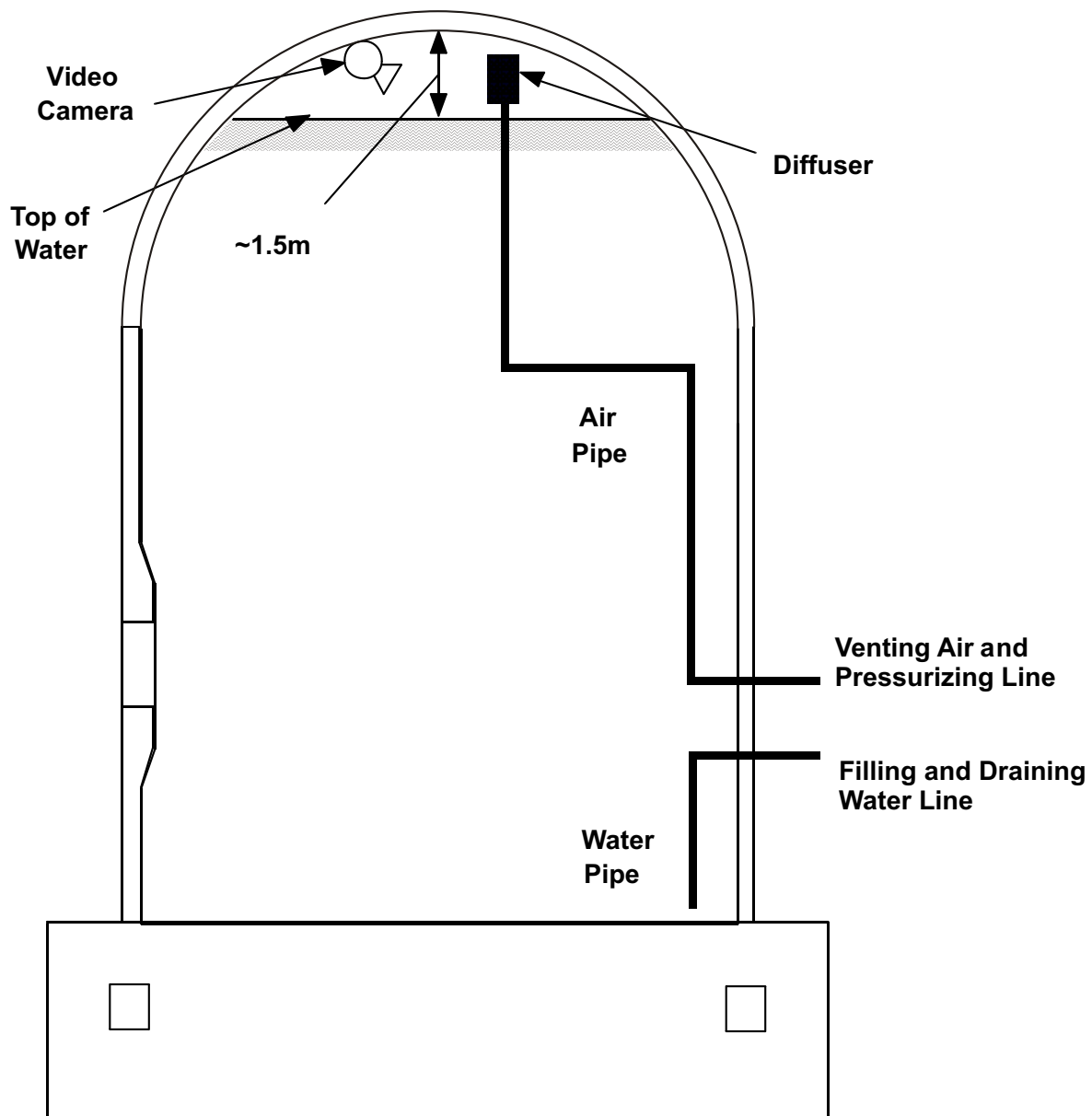


Figure 9-1. PCCV SFMT Pressurization Configuration

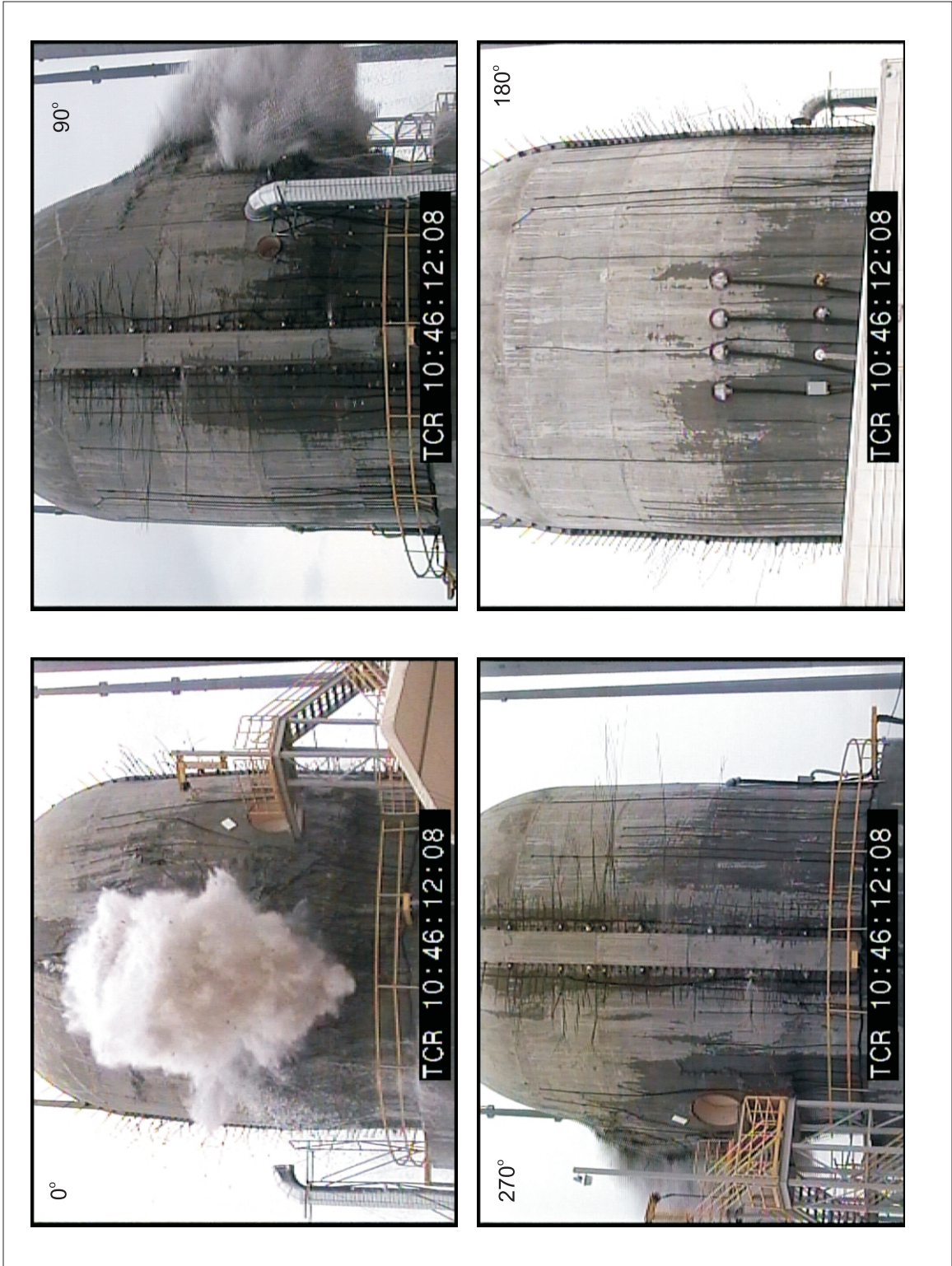


Figure 9-2. PCCV SFMT: Photograph of Exterior of PCCV at Instant of Failure



Figure 9-3. PCCV SFMT: Photograph of Exterior of PCCV After Test

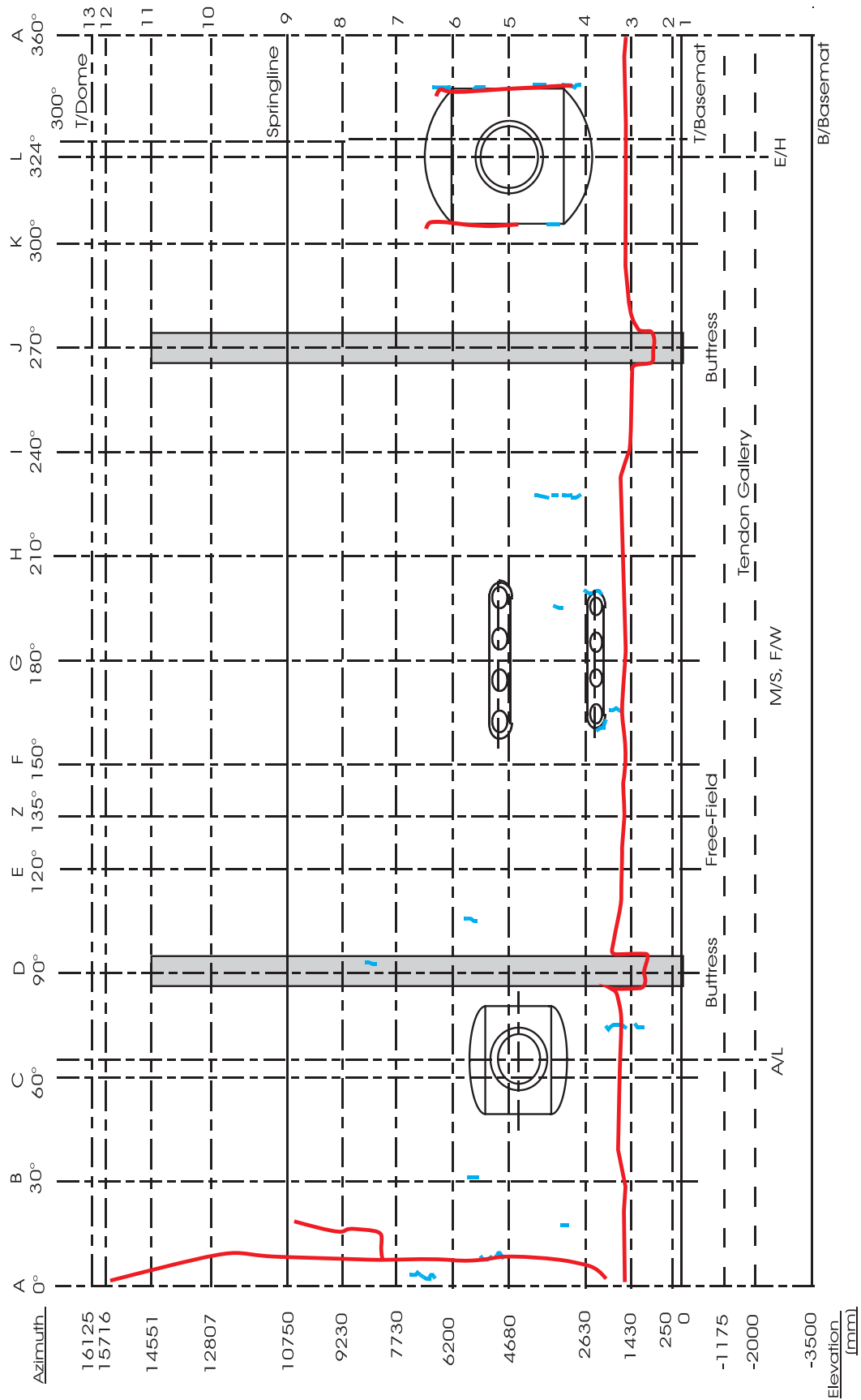


Figure 9-4. PCCV SFMT Rupture Map

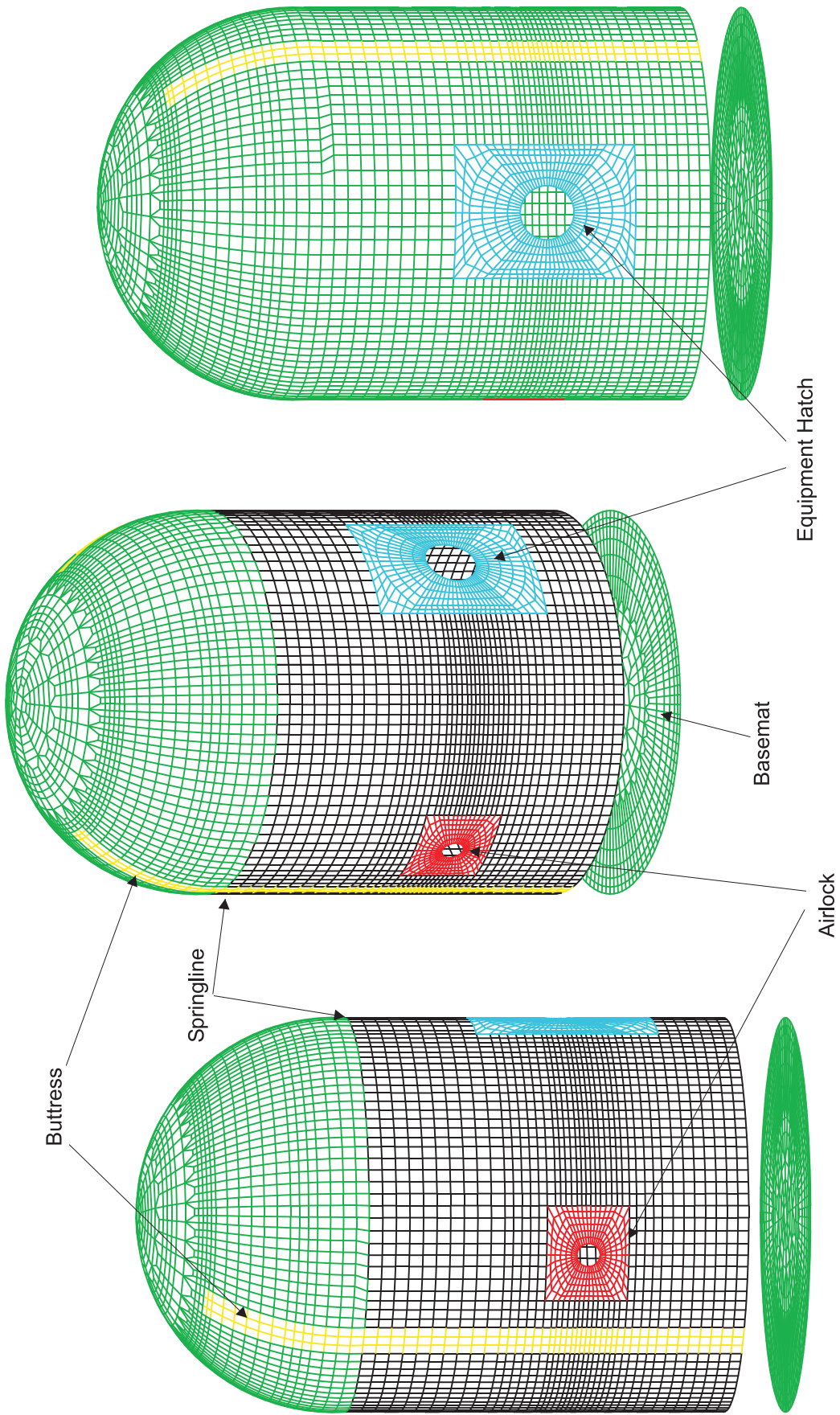
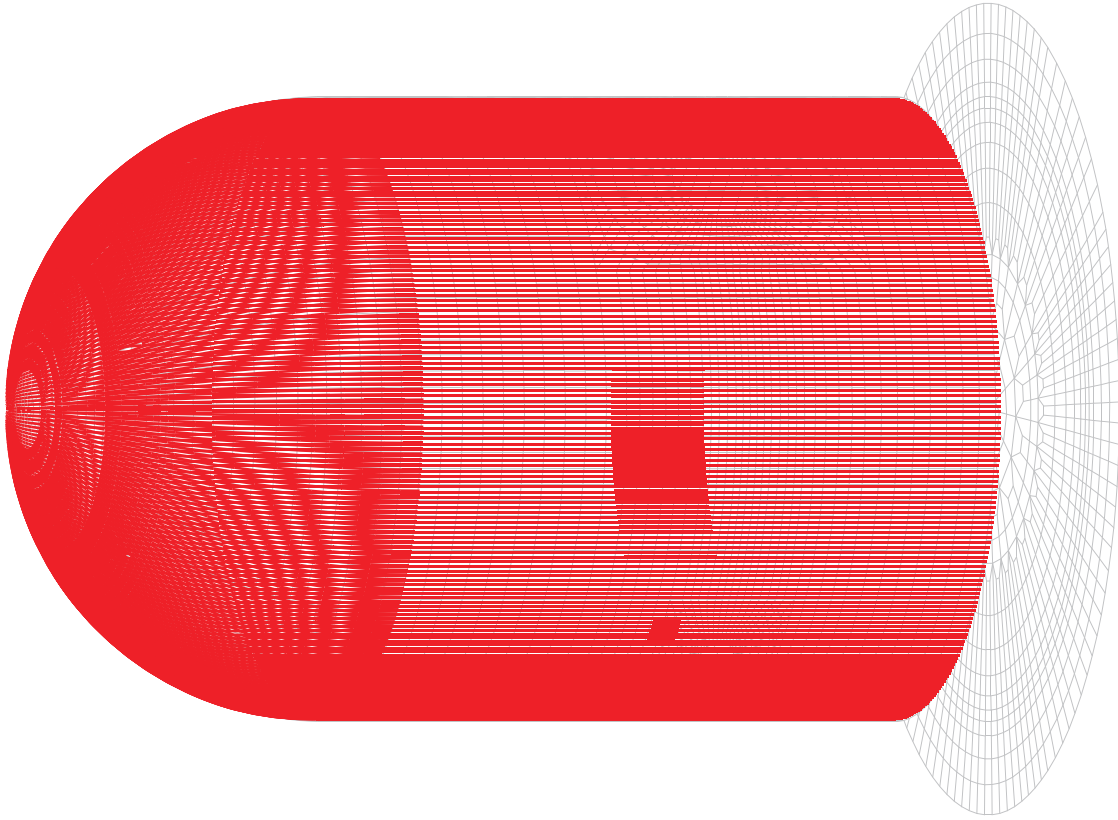


Figure 9-5. PCCV SFMT, 3D Global Shell Model

Inner Row Vertical Reinforcement



Outer Row Vertical Reinforcement

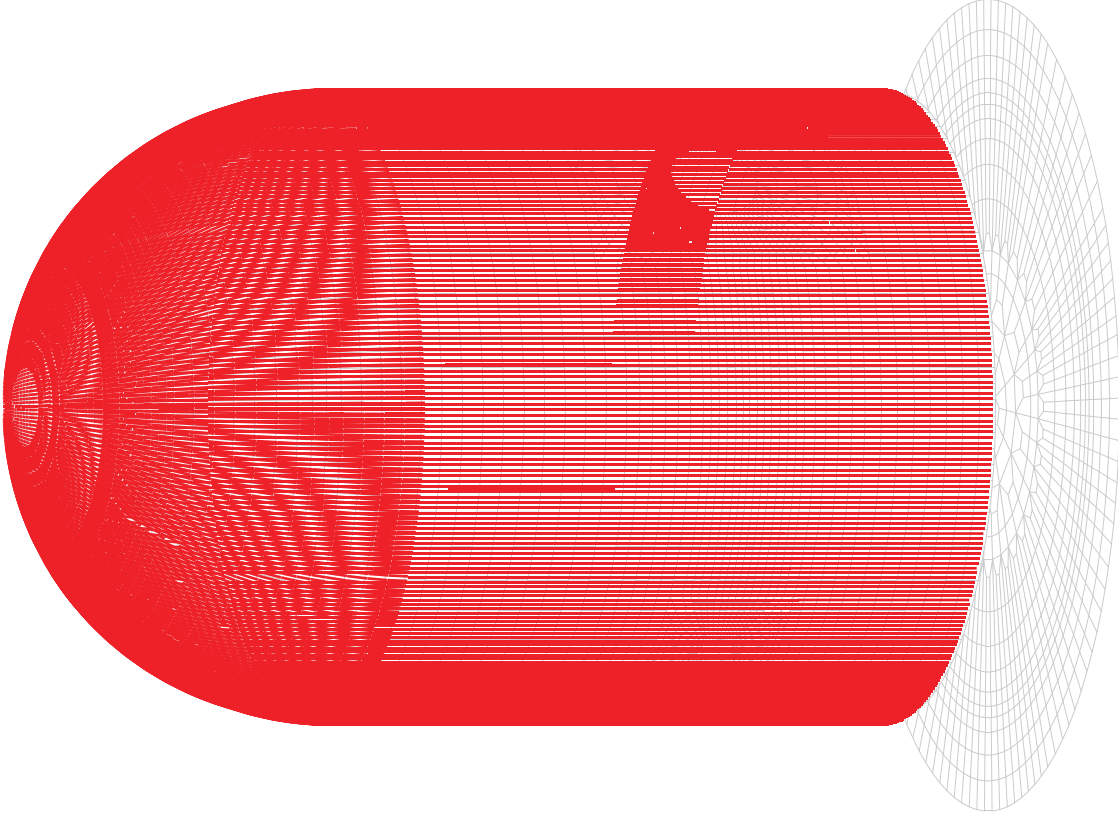
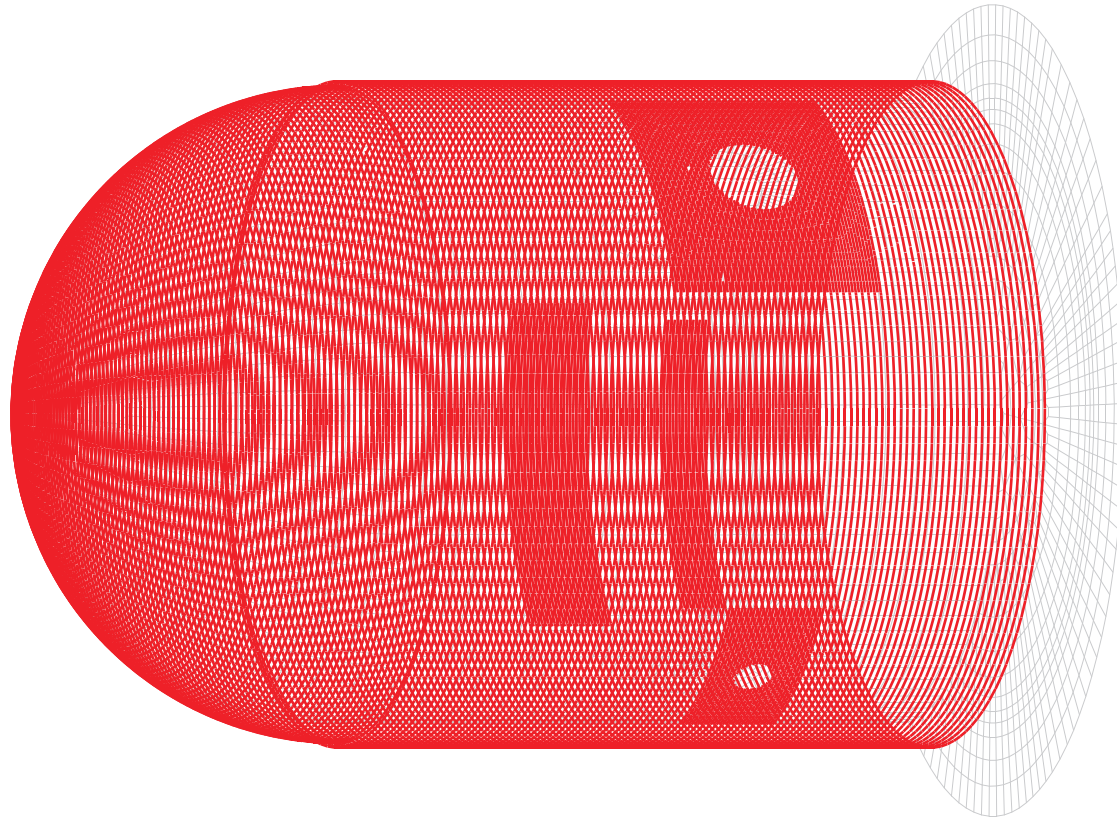


Figure 9-6. PCCV SFMT 3D Global Shell Model, Reinforcement Subelements  
Vertical Reinforcement in Cylinder and Dome

Outer Row Hoop Reinforcement



Inner Row Hoop Reinforcement

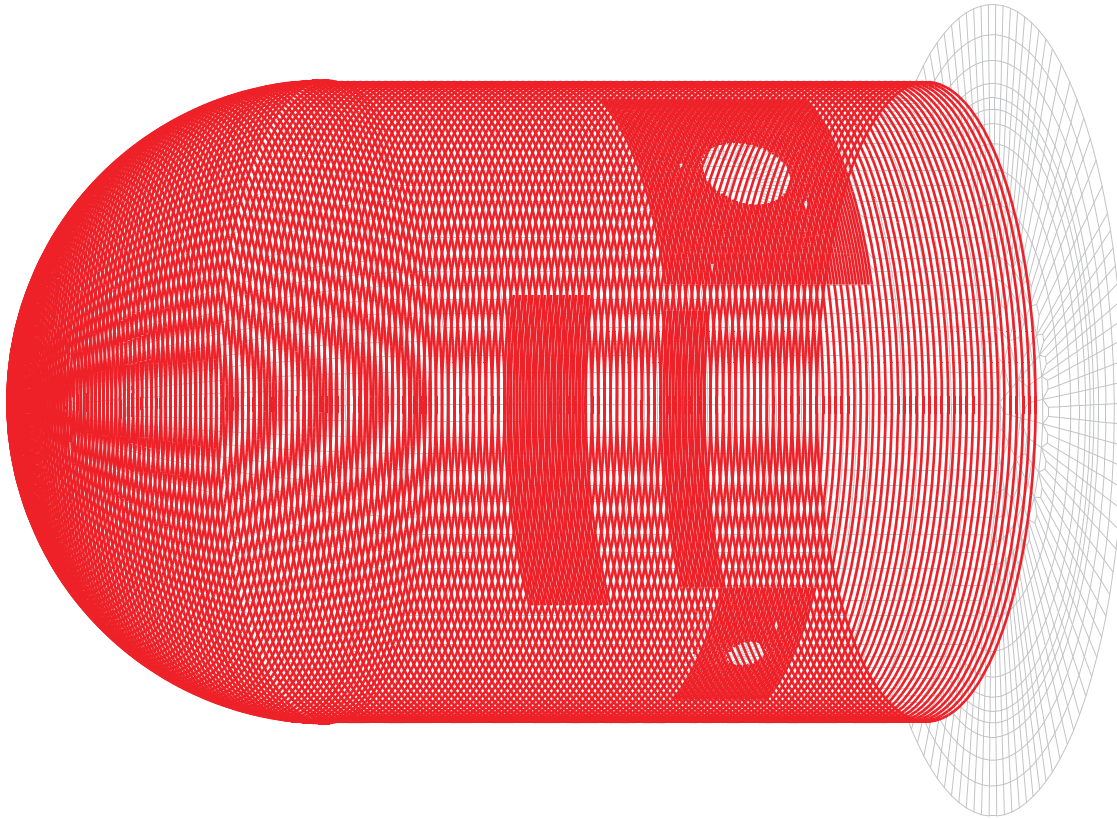


Figure 9-7. PCCV SFMT 3D Global Shell Model, Reinforcement Subelements  
Hoop Reinforcement in Cylinder and Dome

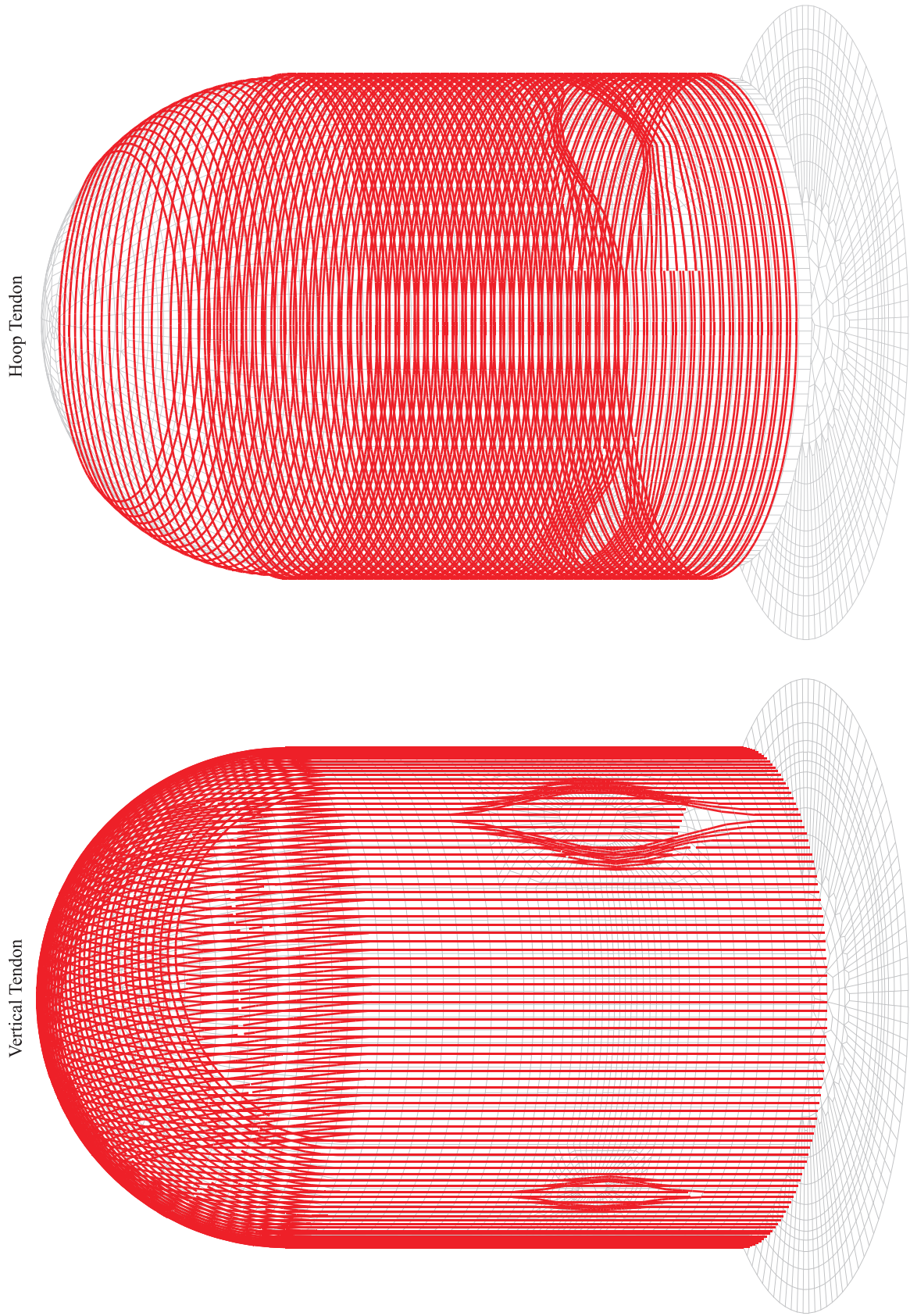
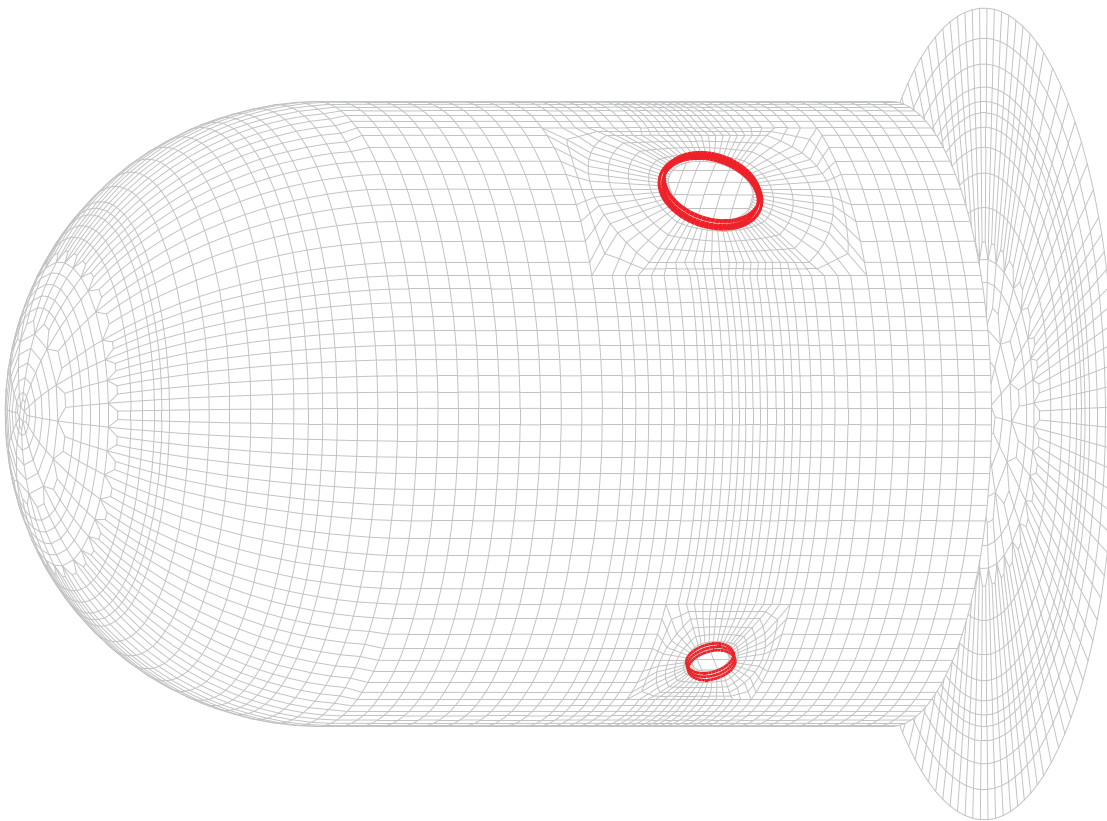


Figure 9-8. PCCV SFMT 3D Global Shell Model, Reinforcement Subelements  
Prestress Tendons in Cylinder and Dome

Air Lock and Equipment Hatch Local Penetration Reinforcement



Buttress Reinforcement

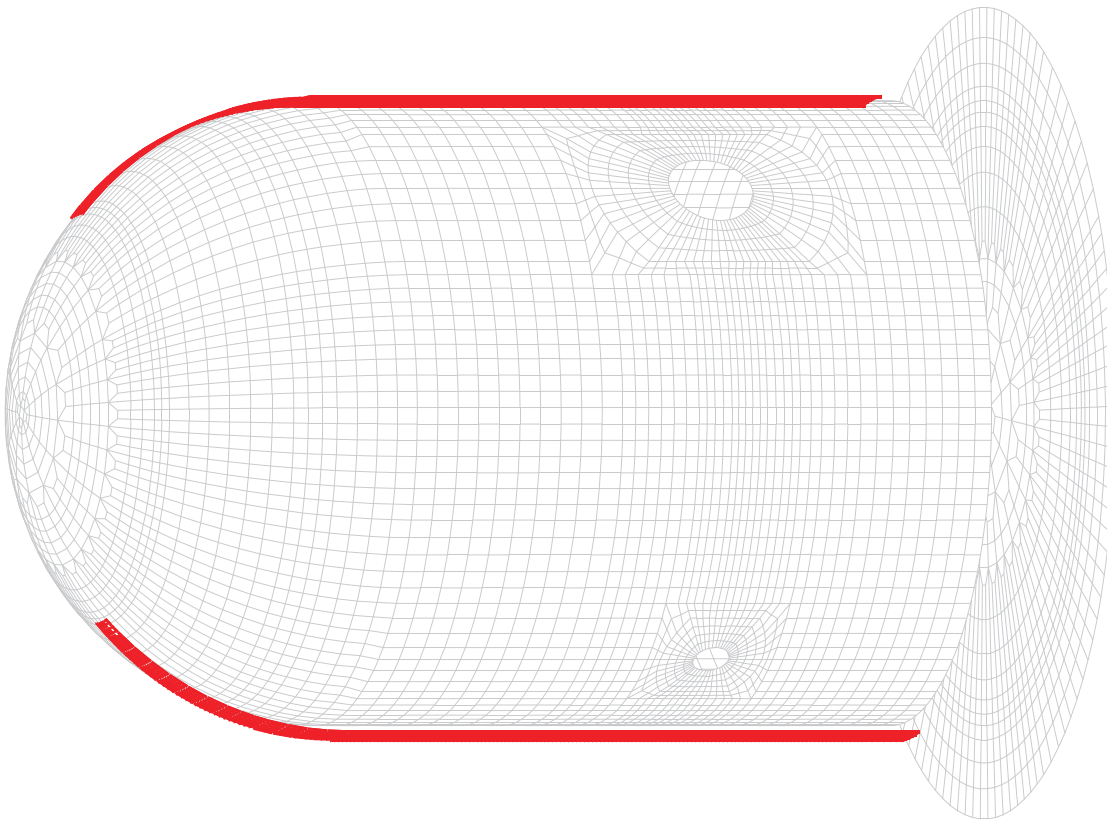


Figure 9-9. PCCV SFMT 3D Global Shell Model, Reinforcement Subelements  
Buttress and Local Penetration Reinforcement

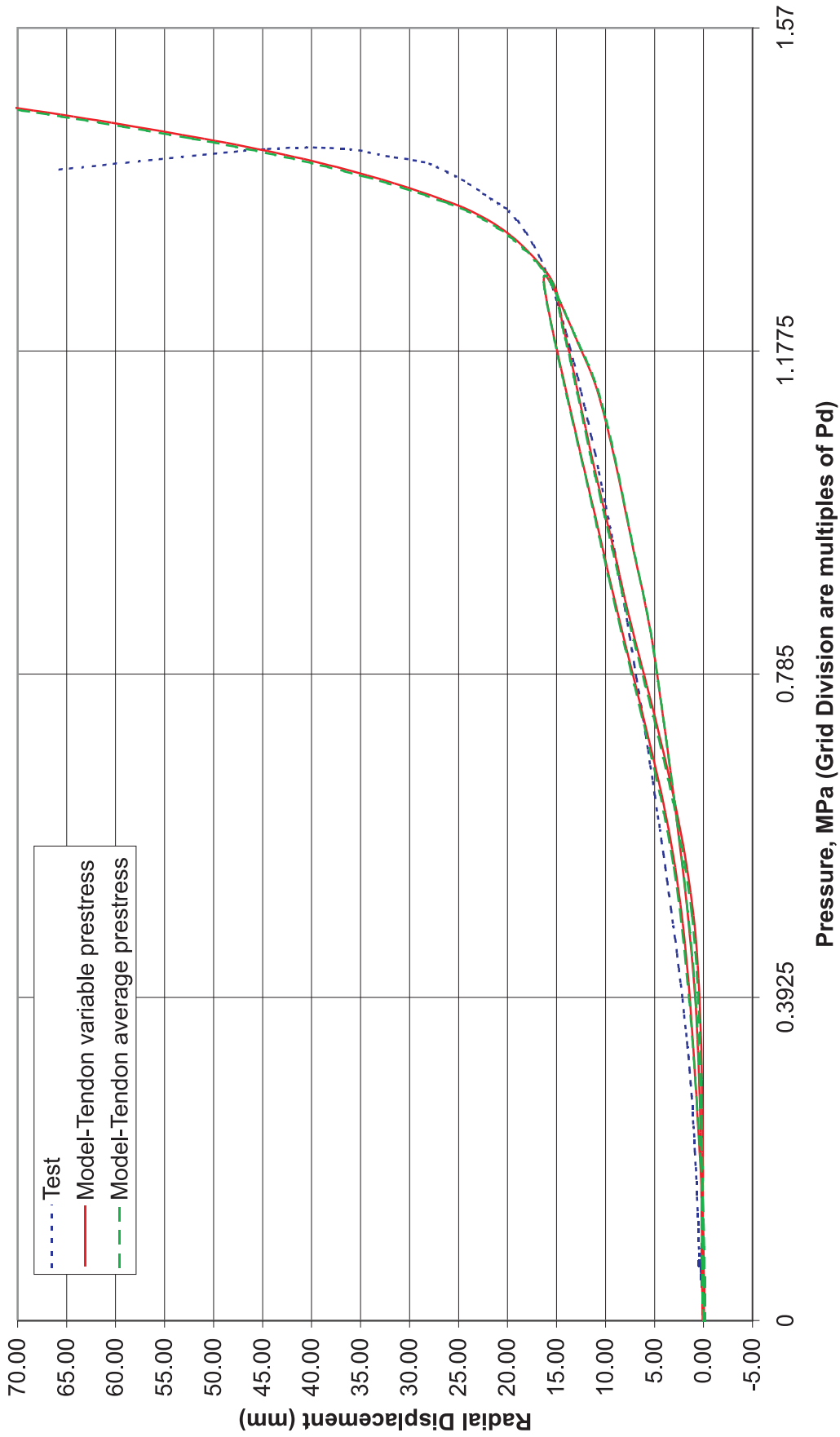


Figure 9-10. PCCV SFMT, 3D Global Shell Model - Gage R-Z4-05 Comparison  
Radial Displacement, 135 Degrees, Elevation 2.63 m

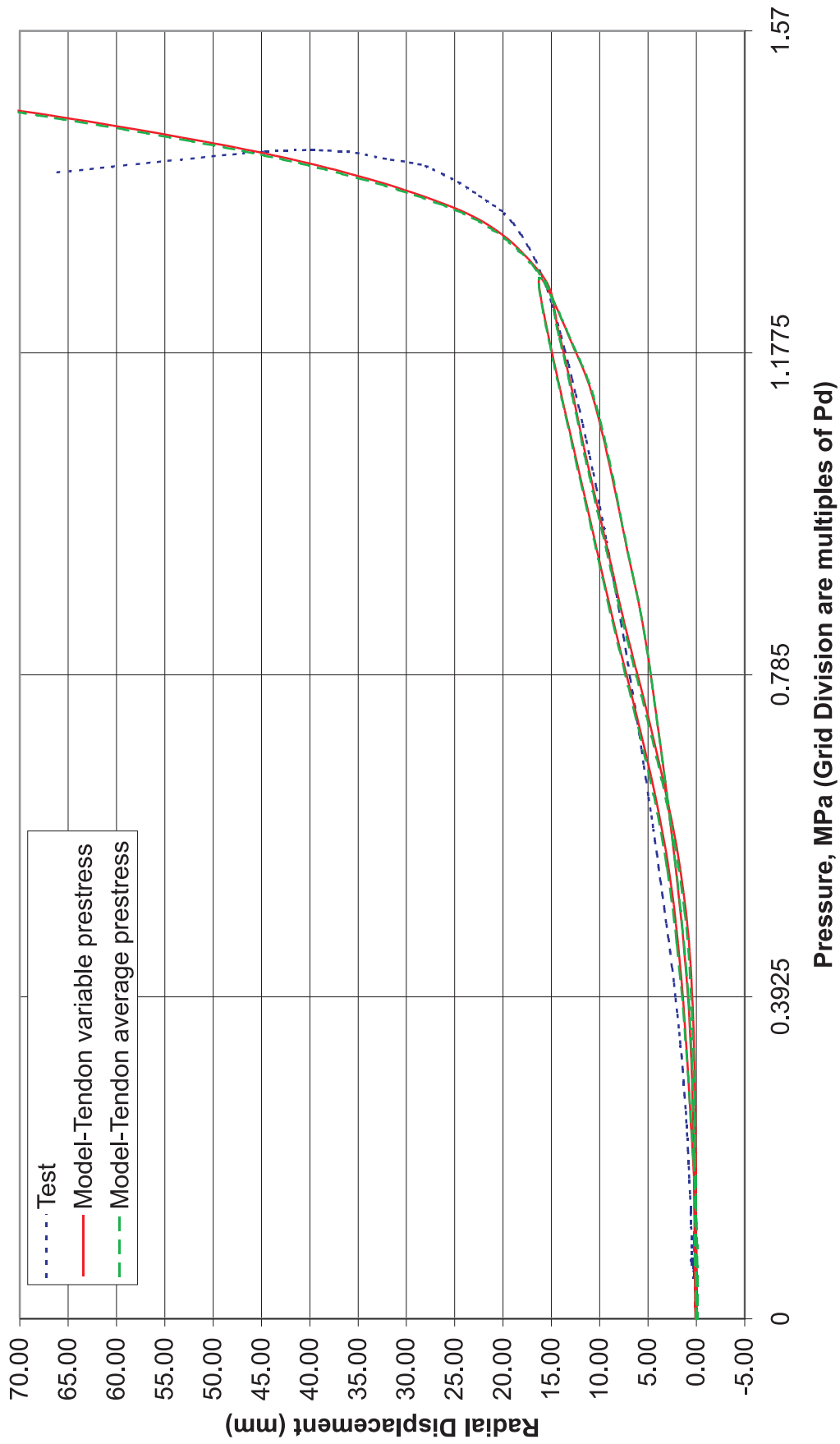


Figure 9-11. PCCV SFMT, 3D Global Shell Model - Gage R-D5-05 Comparison  
Radial Displacement, 90 Degrees Buttress, Elevation 4.68 m

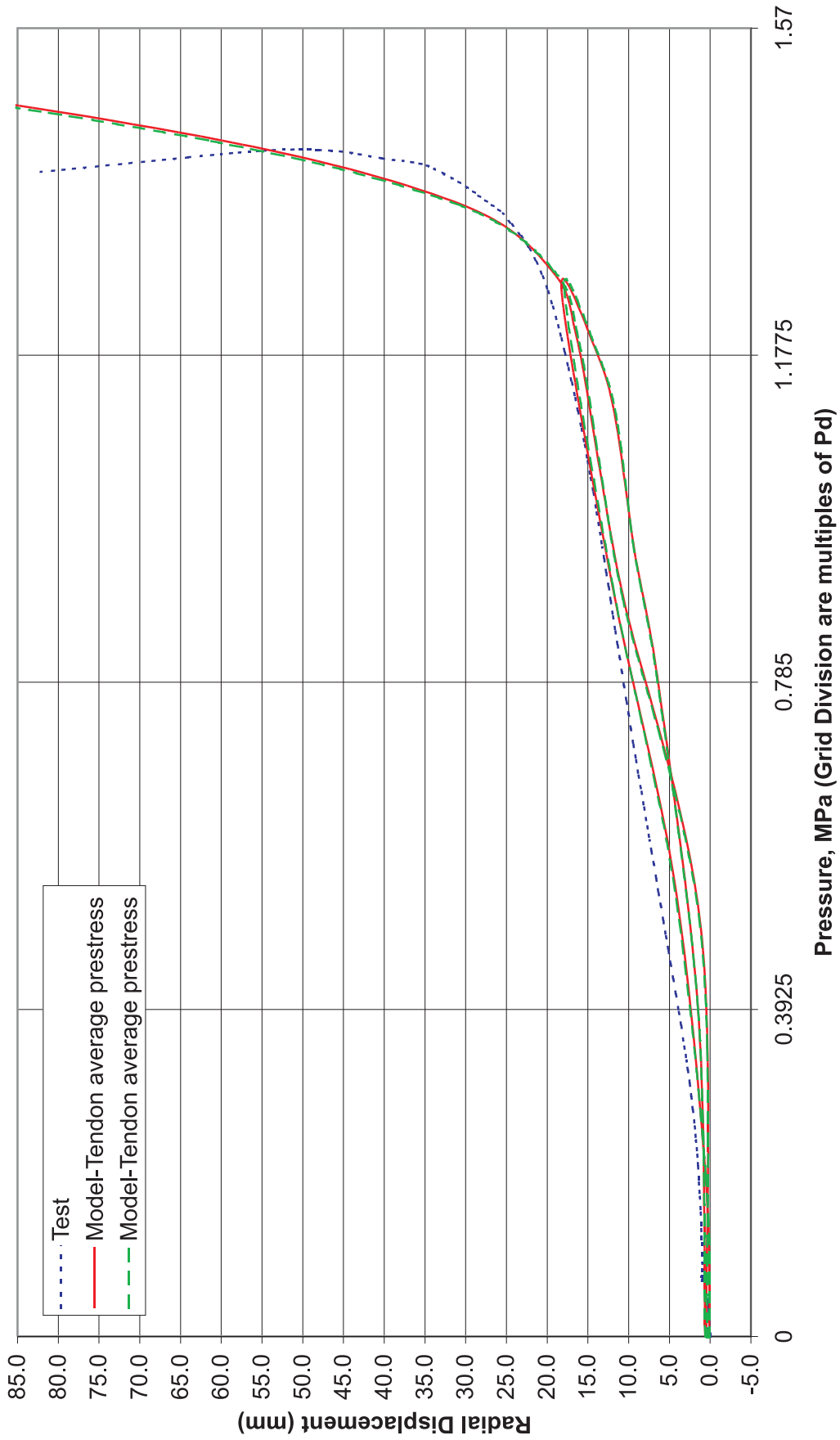


Figure 9-12. PCCV SFMT, 3D Global Shell Model - Gage R-15-05 Comparison  
 Radial Displacement, 240 Degrees, Elevation 4.68 m

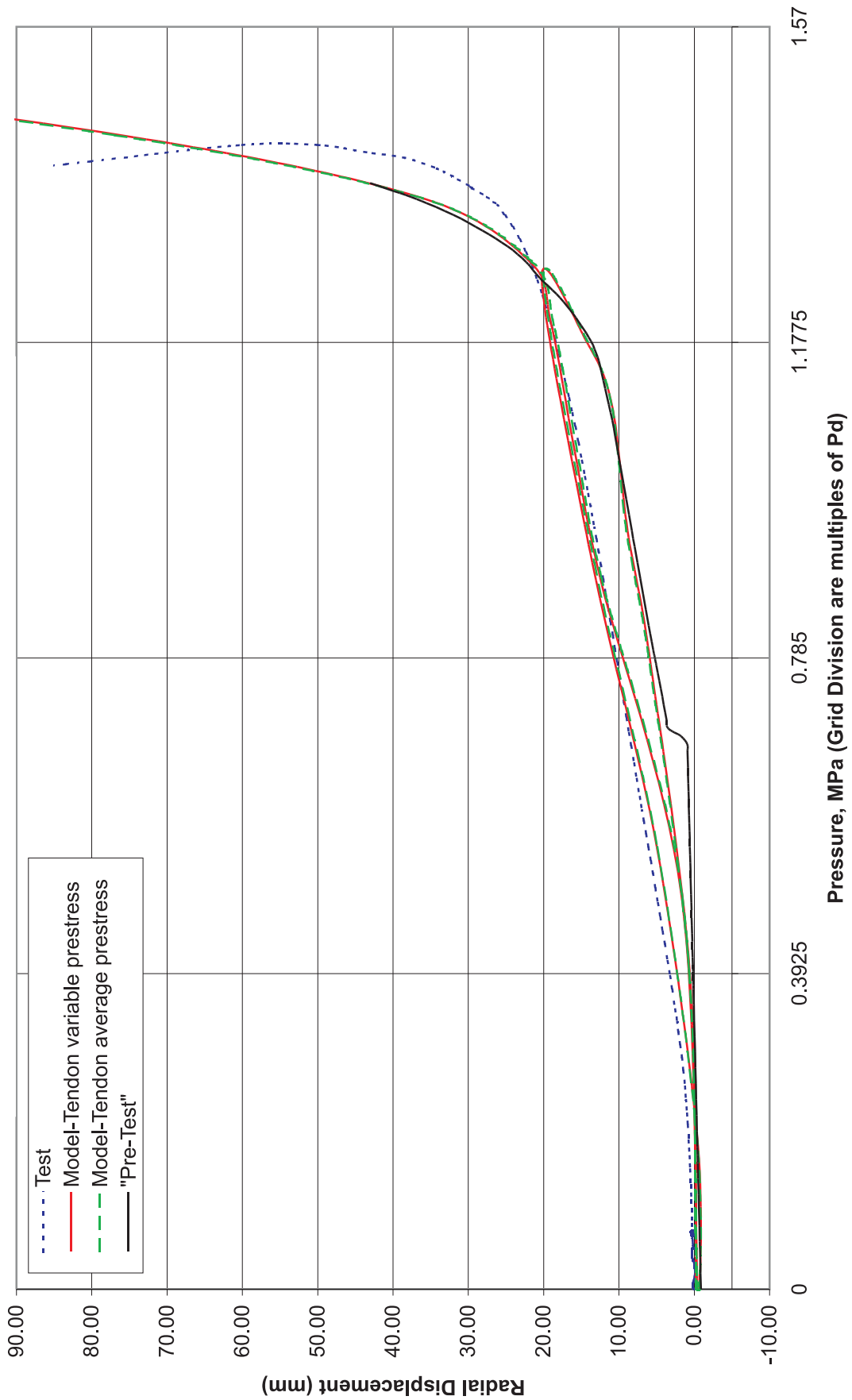


Figure 9-13. PCCV SFMT, 3D Global Shell Model - Gage R-Z6-05 Comparison  
 Radial Displacement, 135 Degrees, Elevation 6.20 m

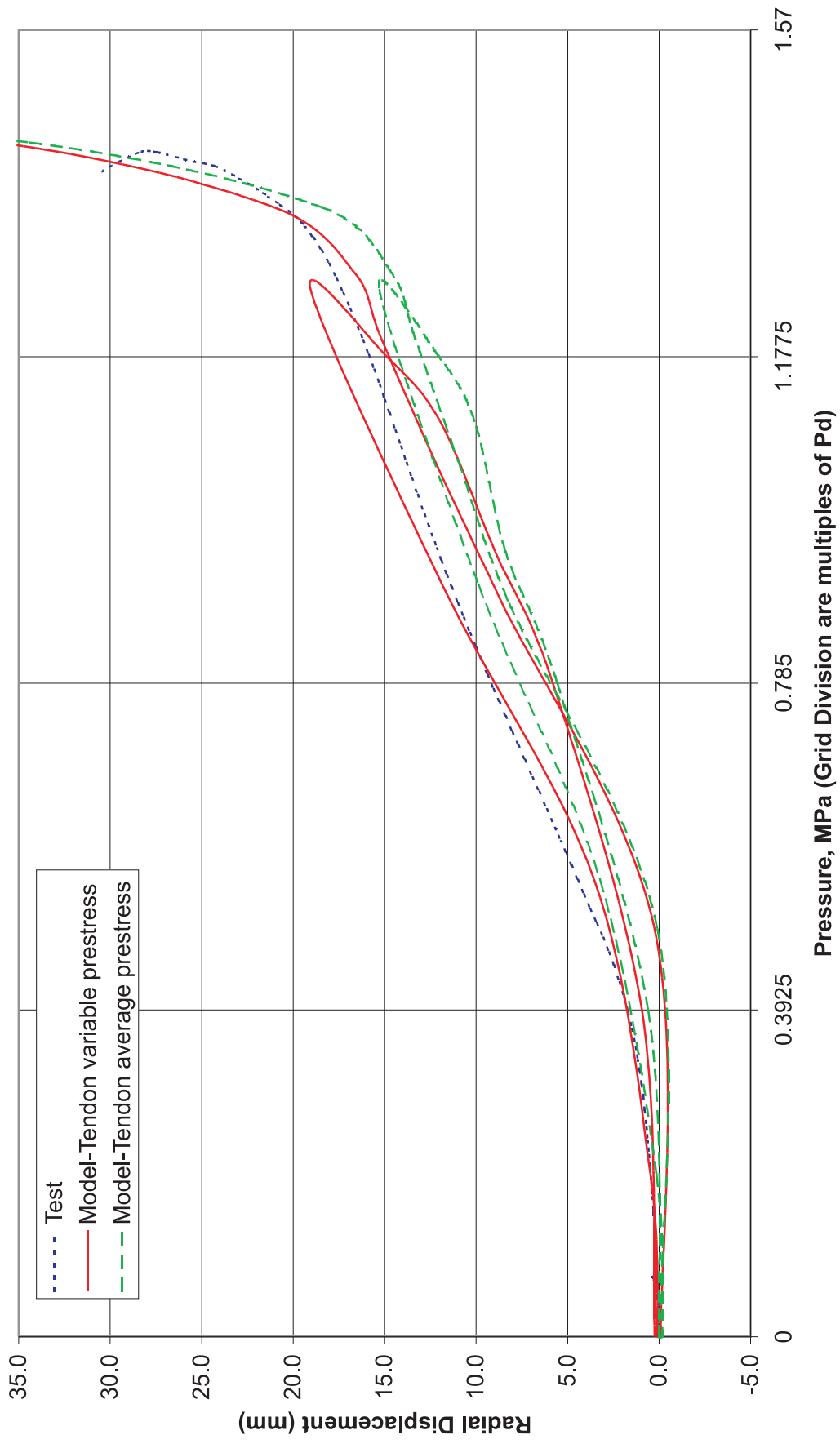


Figure 9-14. PCCV SFMT, 3D Global Shell Model - Gage R-L9-05 Comparison  
 Radial Displacement, 324 Degrees, Elevation 10.75 m Springline

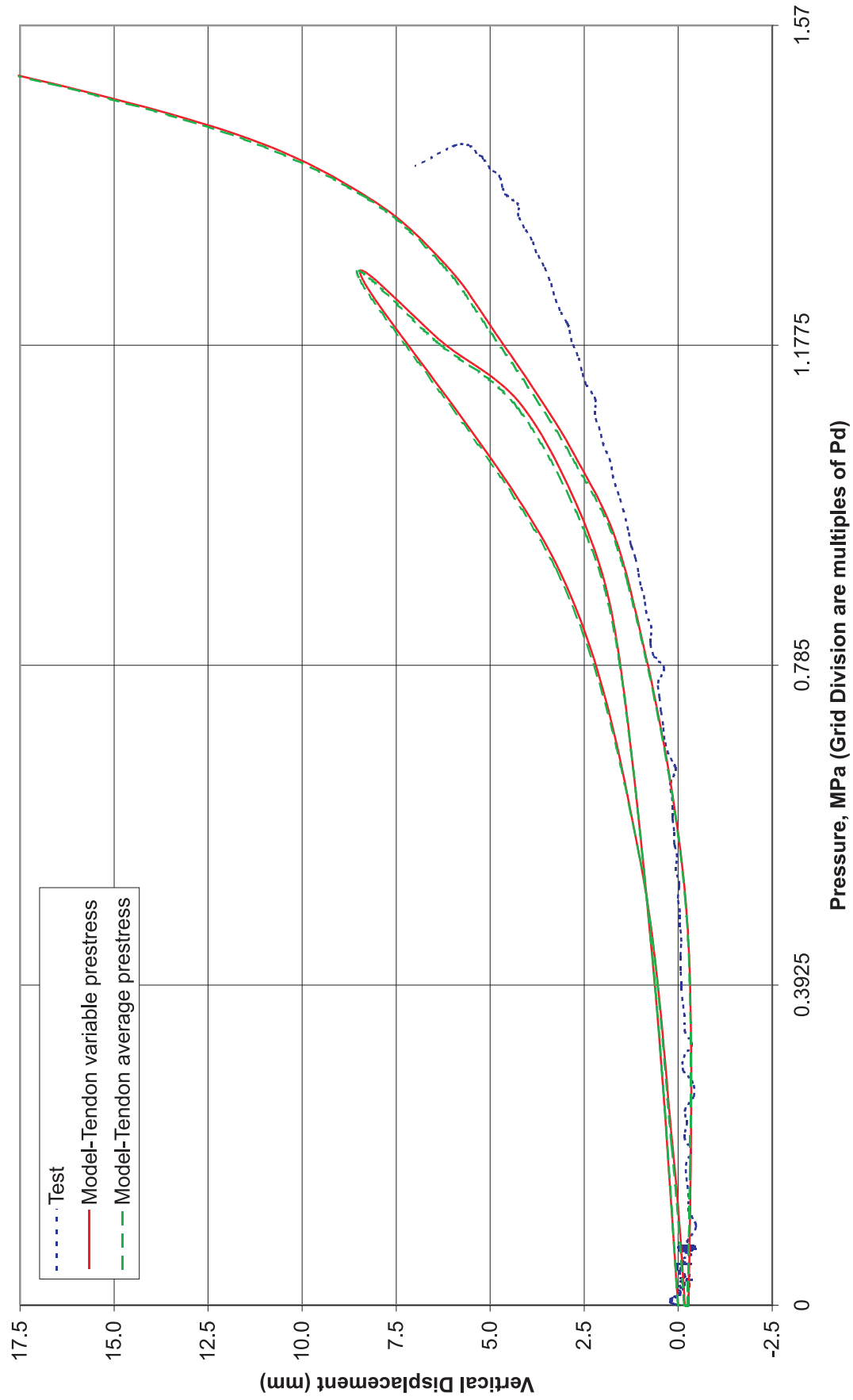


Figure 9-15. PCCV SFMT, 3D Global Shell Model - Gage M-L9-05 Comparison  
 Vertical Displacement, 324 Degrees, Elevation 10.75 m Springline

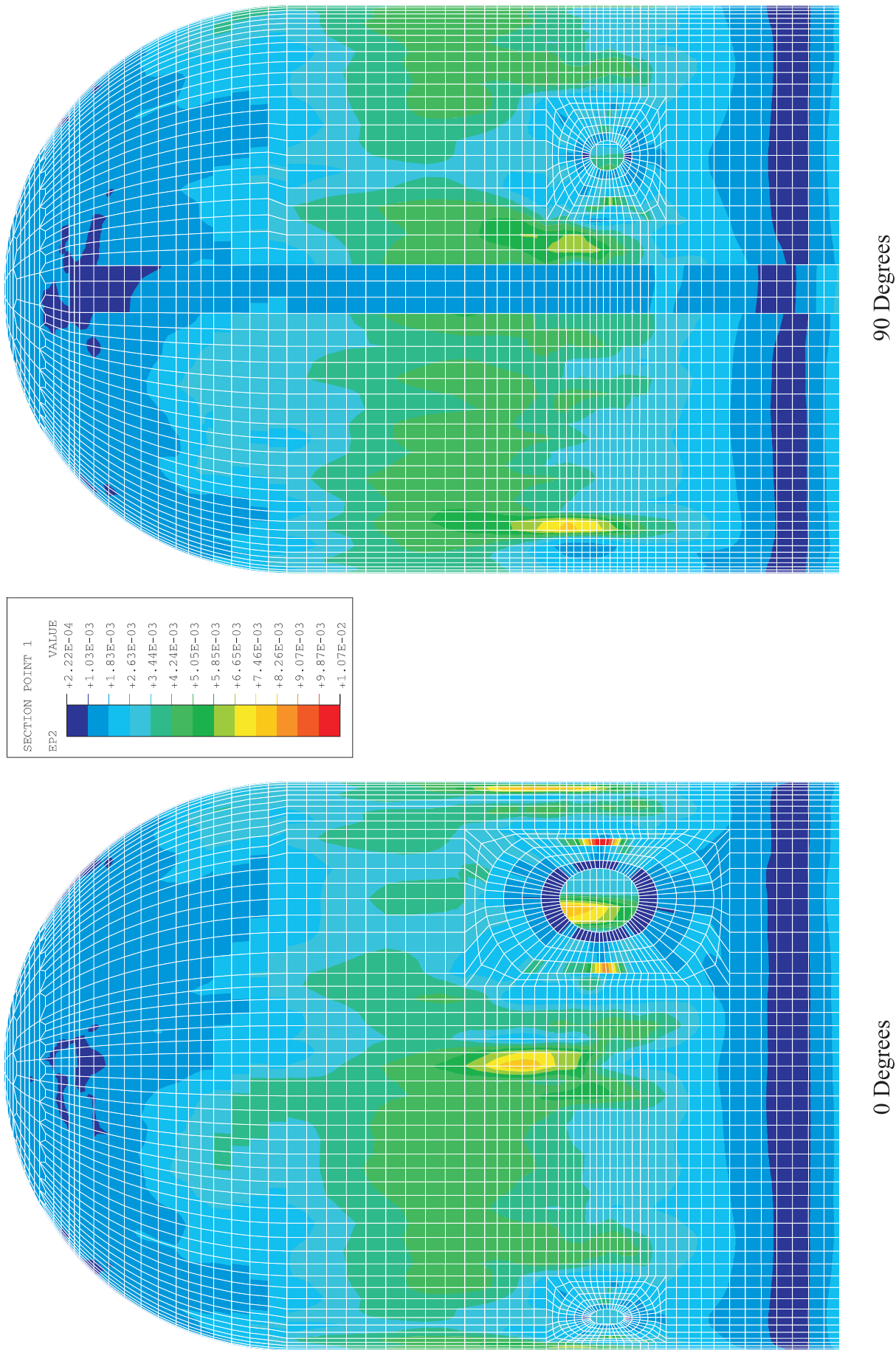


Figure 9-16. PCCV SFMT, 3D Global Shell Model. Liner Maximum Principal Strain.  
For Azimuth: 0 and 90 Degrees at 1.279 MPa (3.25 Pd)

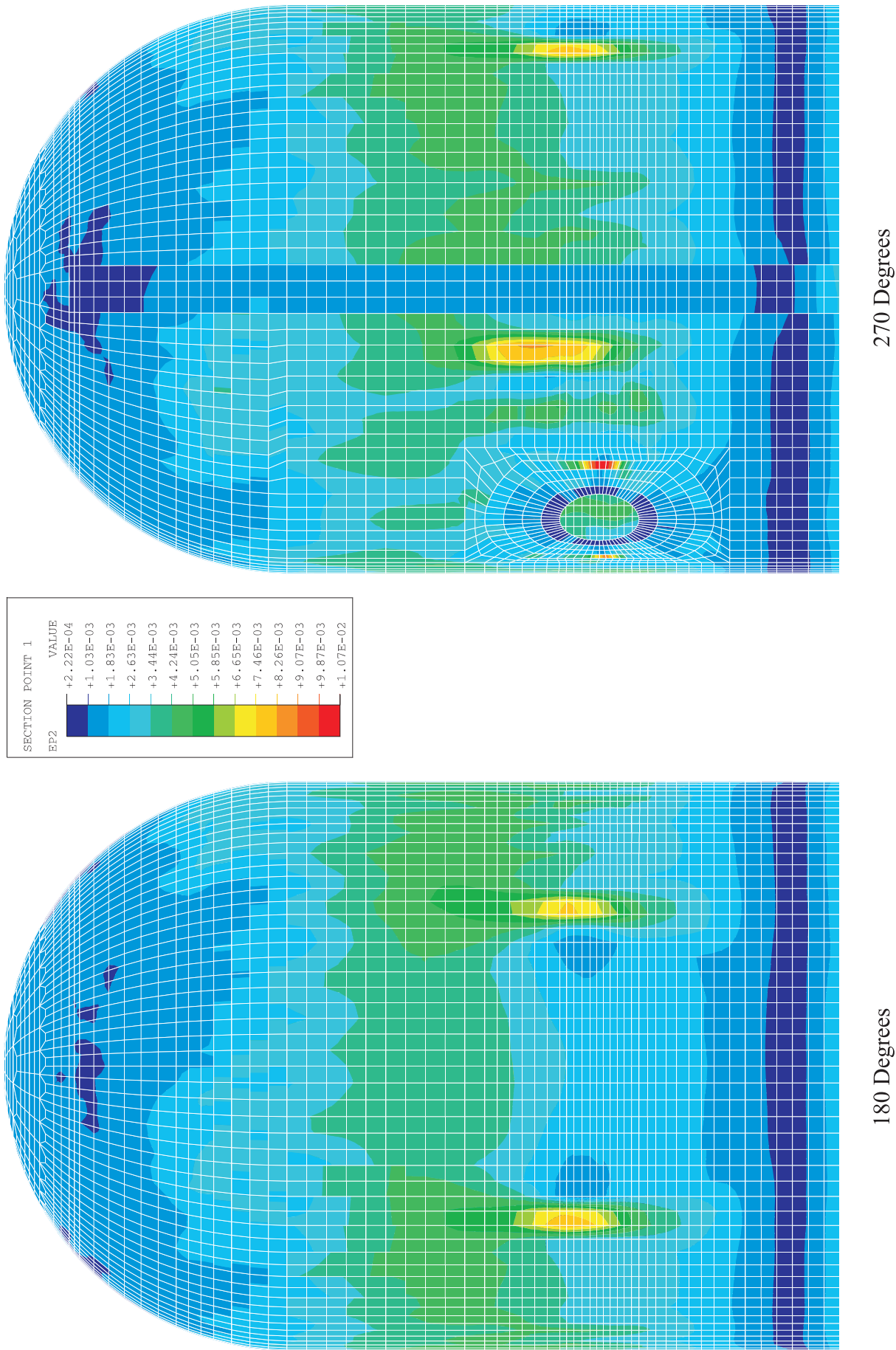
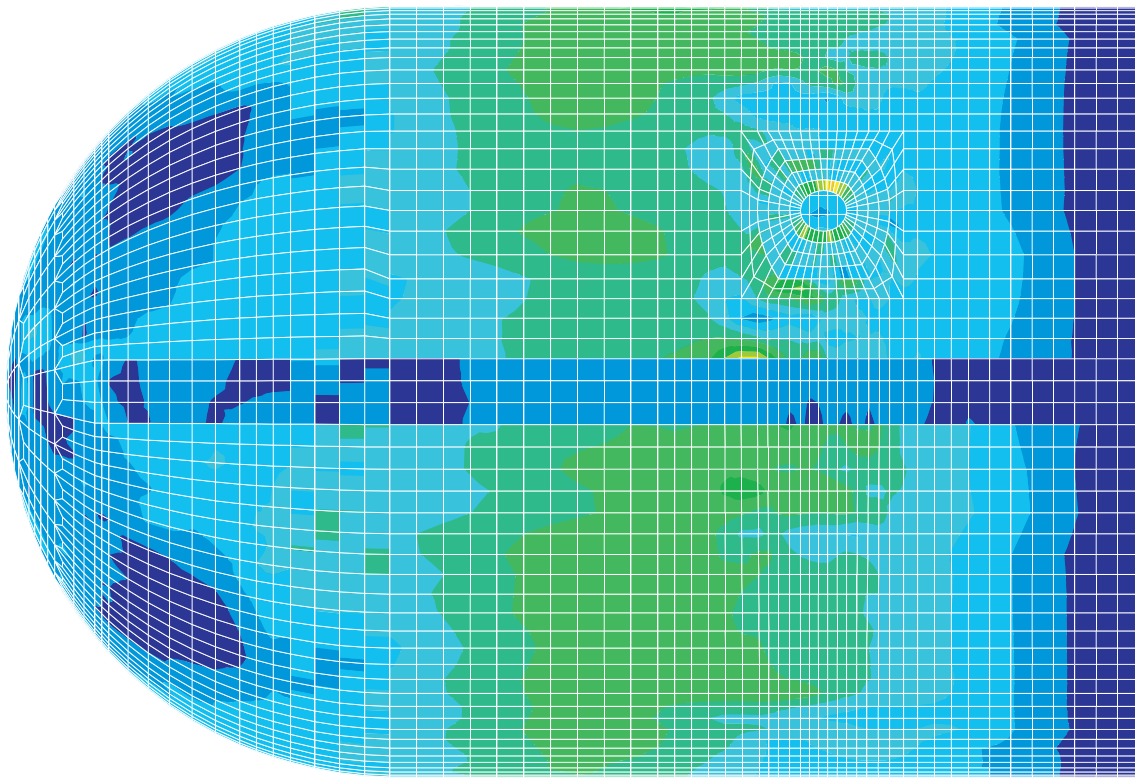
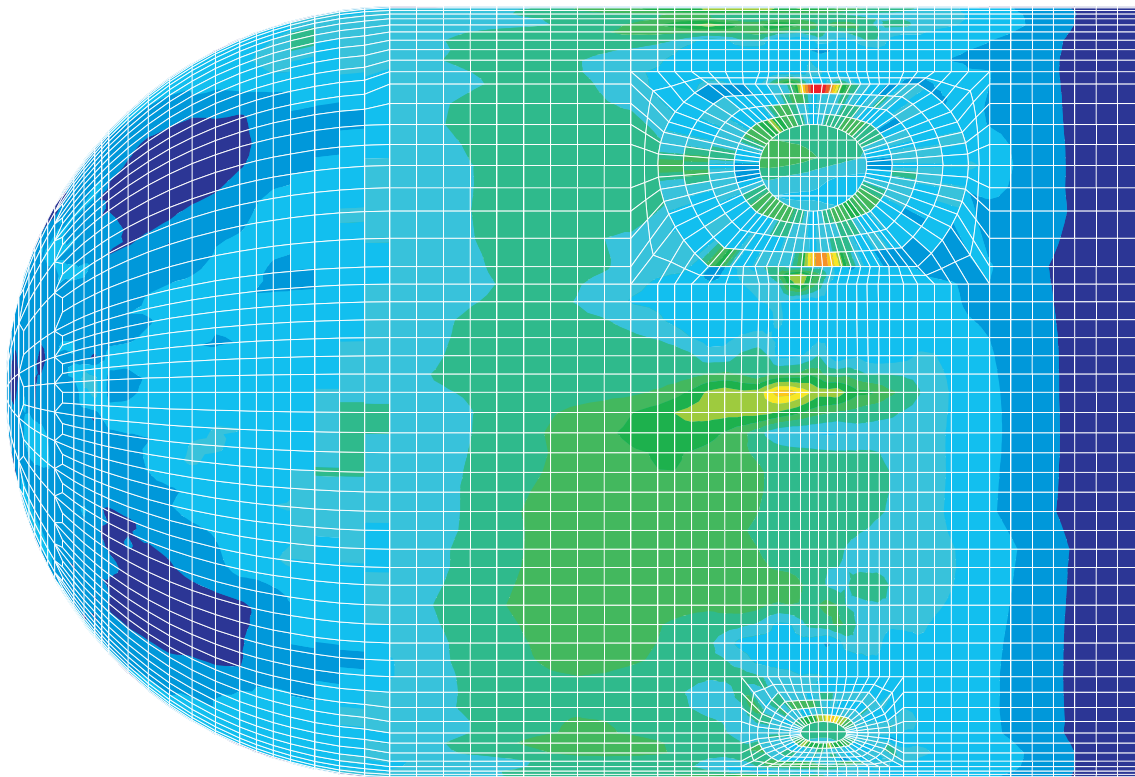
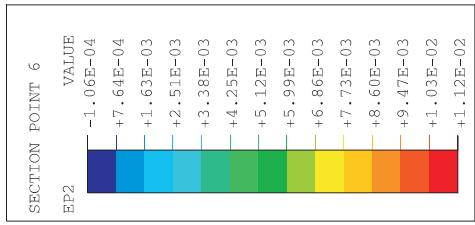


Figure 9-17. PCCV SFMT, 3D Global Shell Model. Liner Maximum Principal Strain. For Azimuth: 180 and 270 Degrees at 1.279 MPa (3.25 Pd)

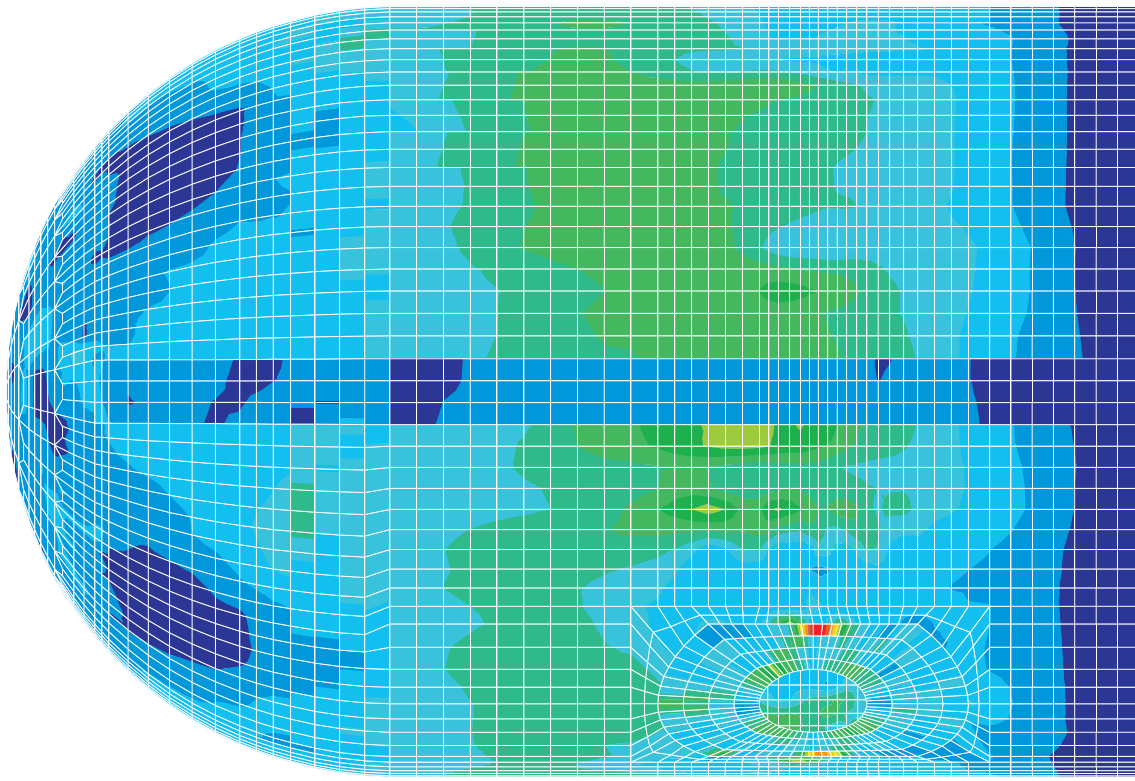


90 Degrees



0 Degrees

Figure 9-18. PCCV SFMT, 3D Global Shell Model. Concrete Maximum Principal Strain. For Azimuth: 0 and 90 Degrees at 1.279 MPa (3.25 Pd)



180 Degrees

270 Degrees

Figure 9-19. PCCV SFMT, 3D Global Shell Model. Concrete Maximum Principal Strain.  
For Azimuth: 180 and 270 Degrees at 1.279 MPa (3.25 Pd)

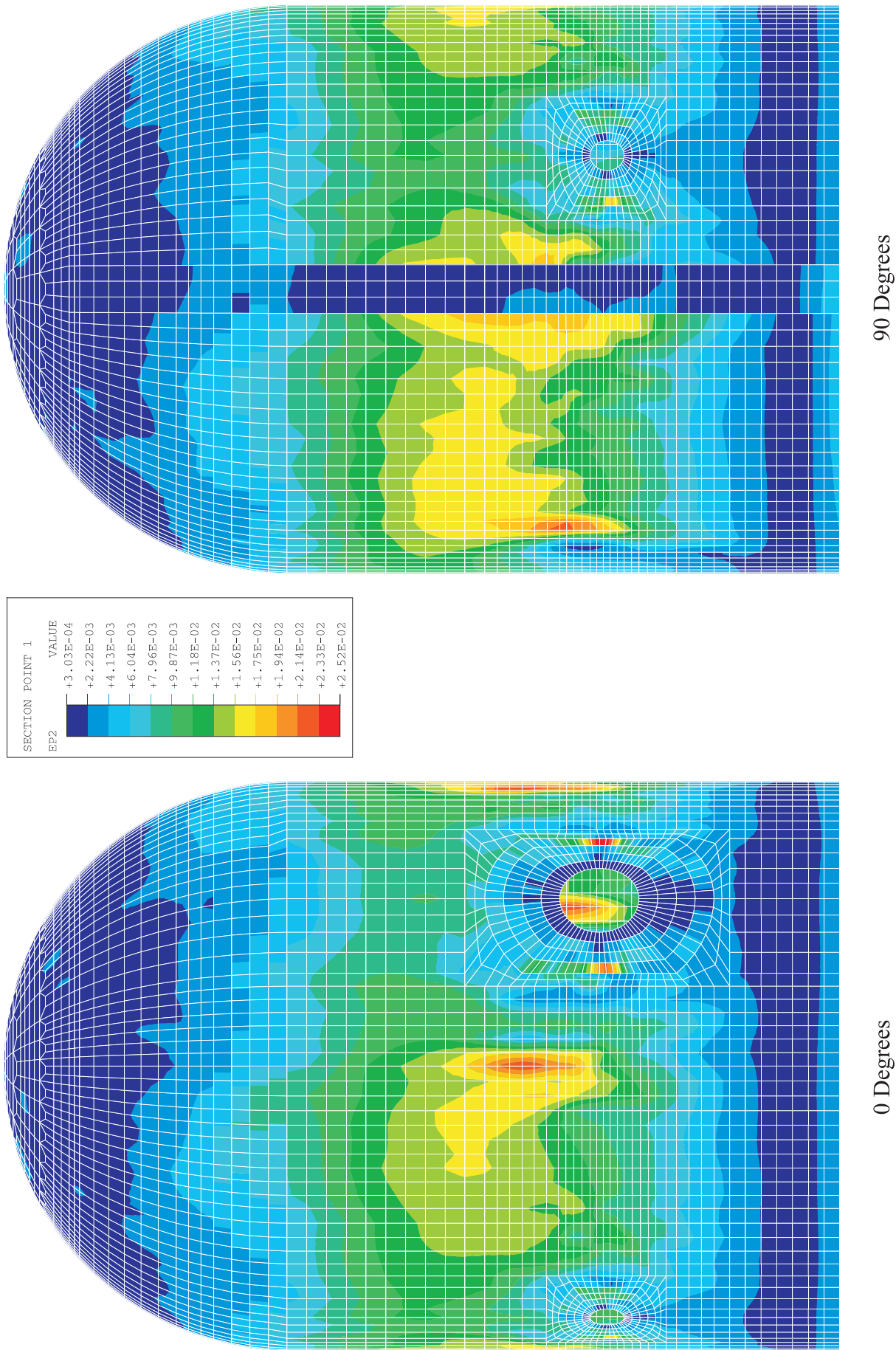
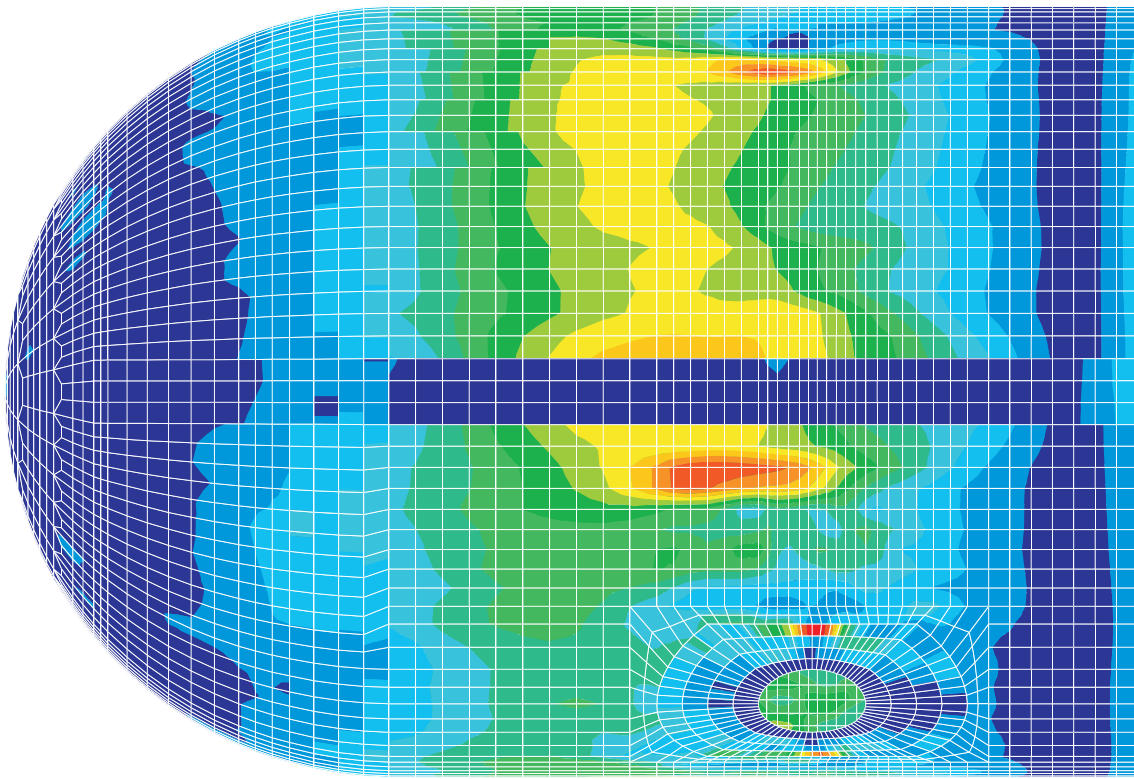


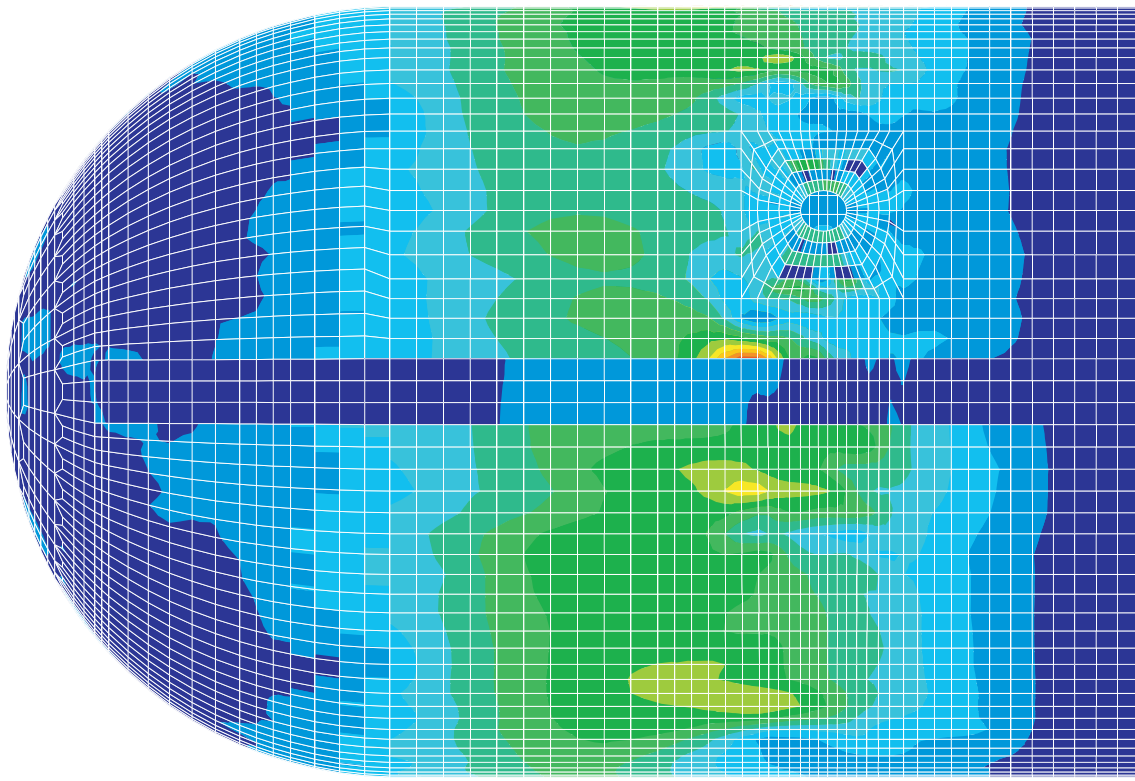
Figure 9-20. PCCV SFMT, 3D Global Shell Model. Liner Maximum Principal Strain. For Azimuth: 0 and 90 Degrees at 1.437 MPa (3.65 Pd)



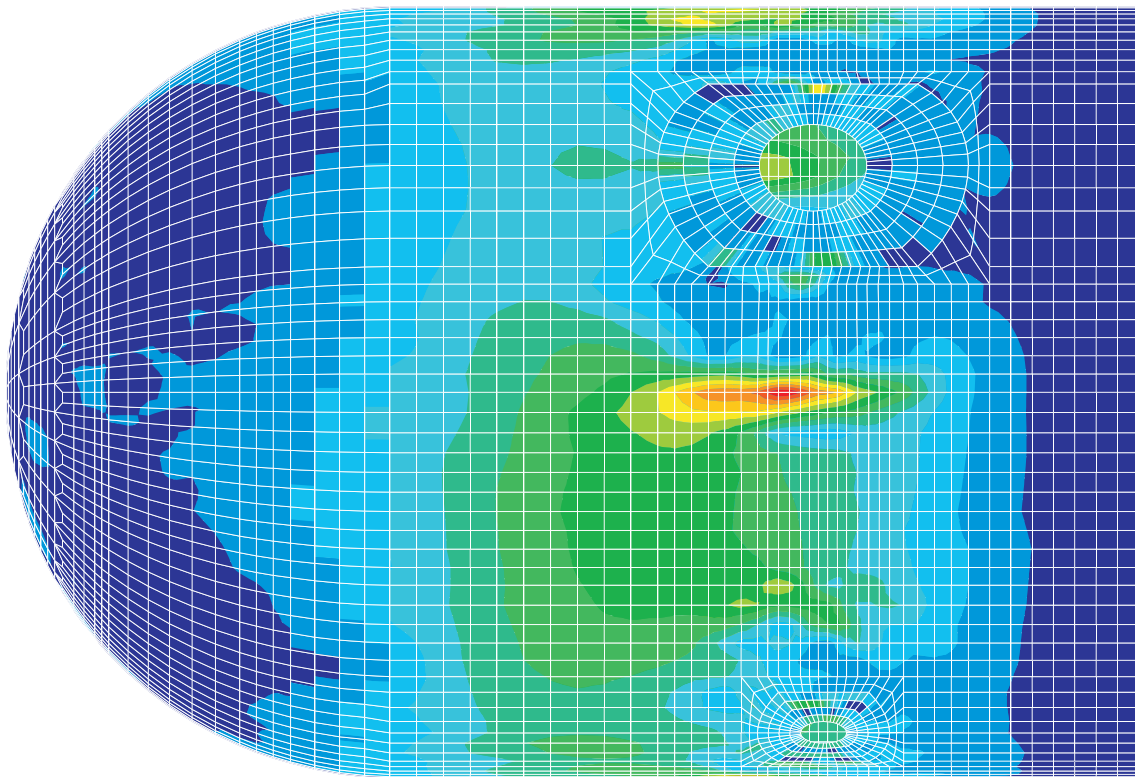
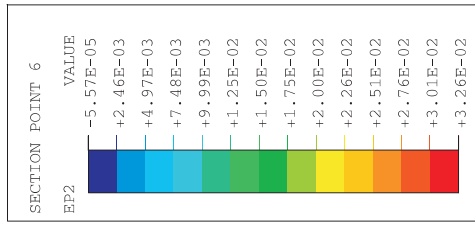
180 Degrees

270 Degrees

Figure 9-21. PCCV SFMT, 3D Global Shell Model. Liner Maximum Principal Strain.  
For Azimuth: 180 and 270 Degrees at 1.437 MPa (3.65 Pd)

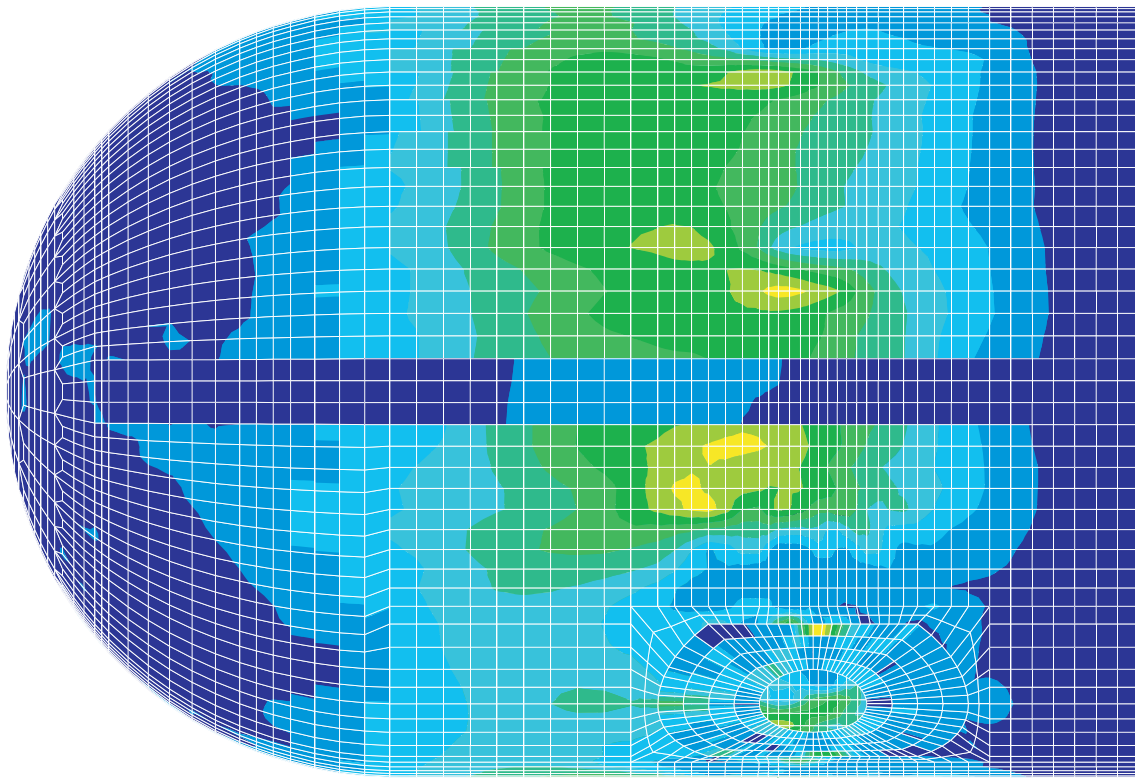


90 Degrees

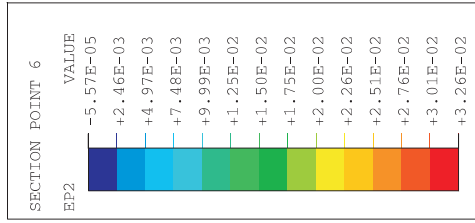


0 Degrees

Figure 9-22. PCCV SFMT, 3D Global Shell Model. Concrete Maximum Principal Strain. For Azimuth: 0 and 90 Degrees at 1.437 MPa (3.65 Pd)



180 Degrees



270 Degrees

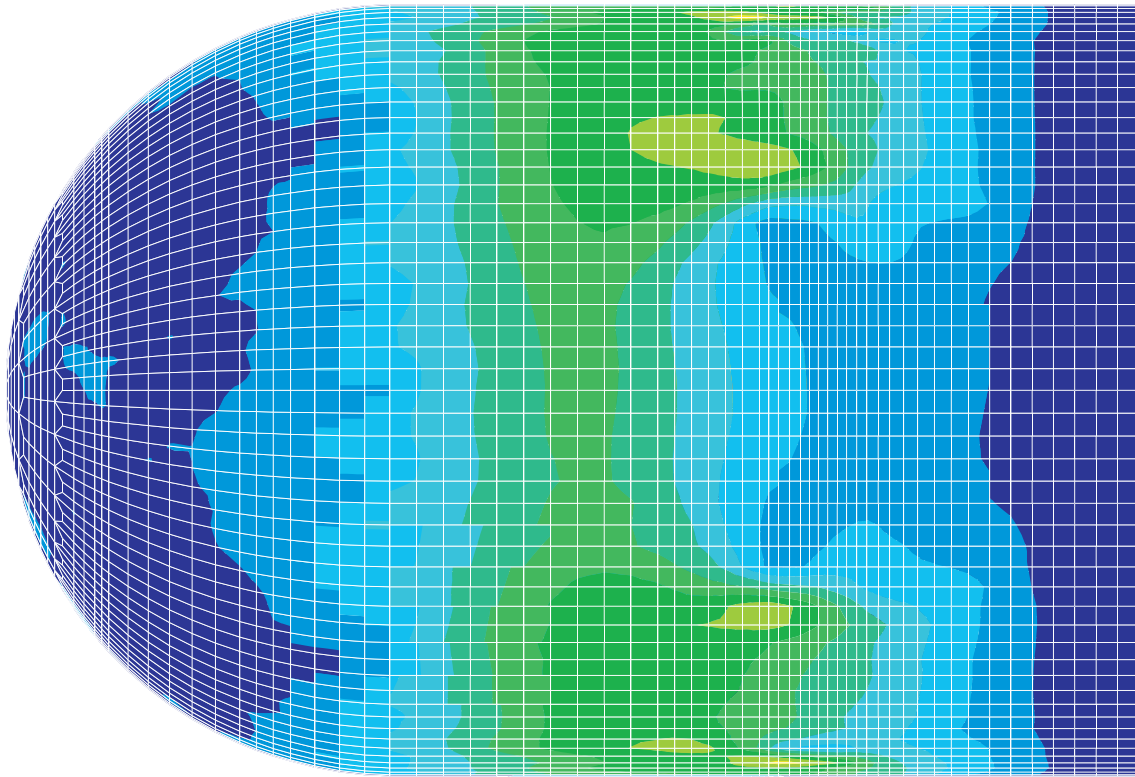
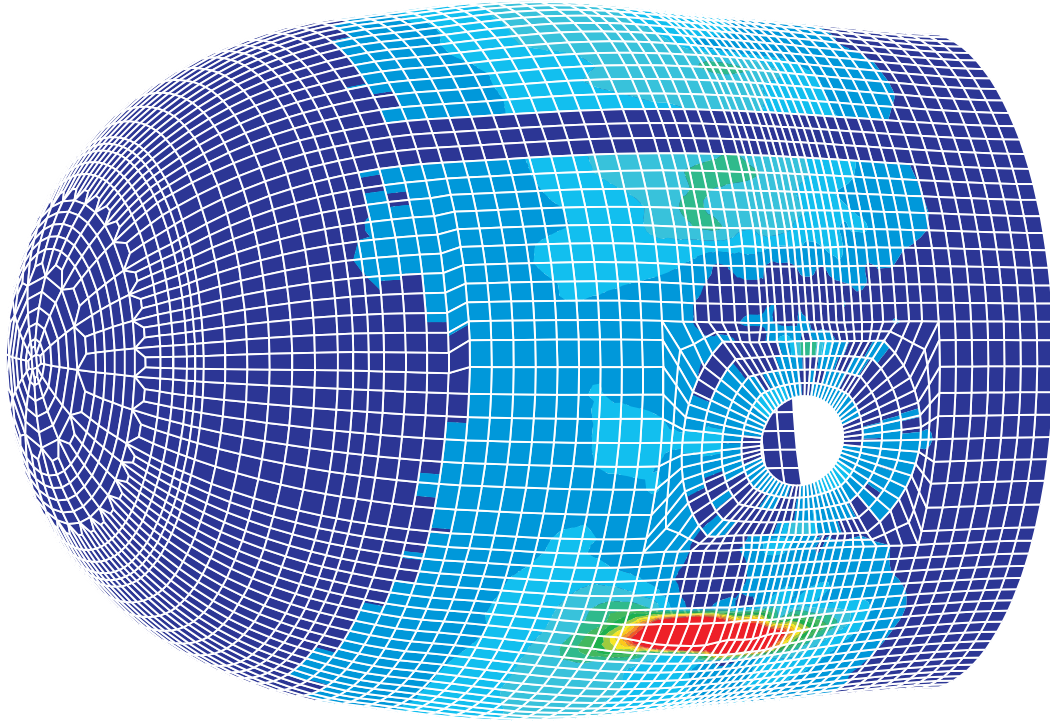
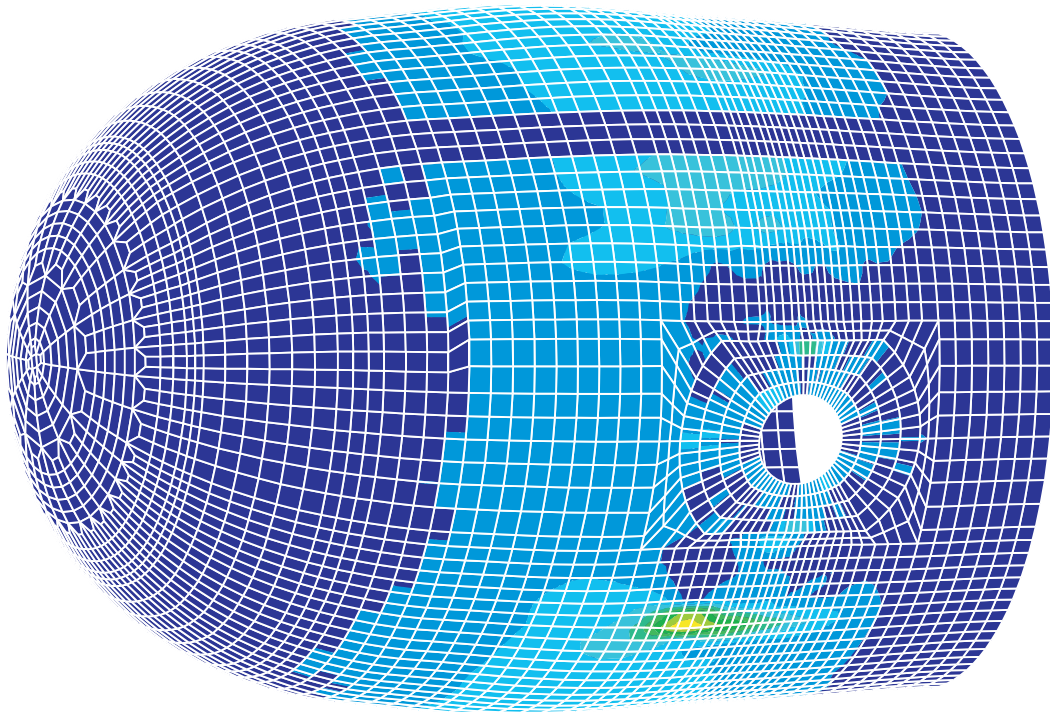
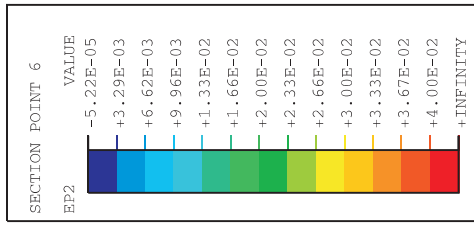


Figure 9-23. PCCV SFMT, 3D Global Shell Model. Concrete Maximum Principal Strain.  
For Azimuth: 180 and 270 Degrees at 1.437 MPa (3.65 Pd)

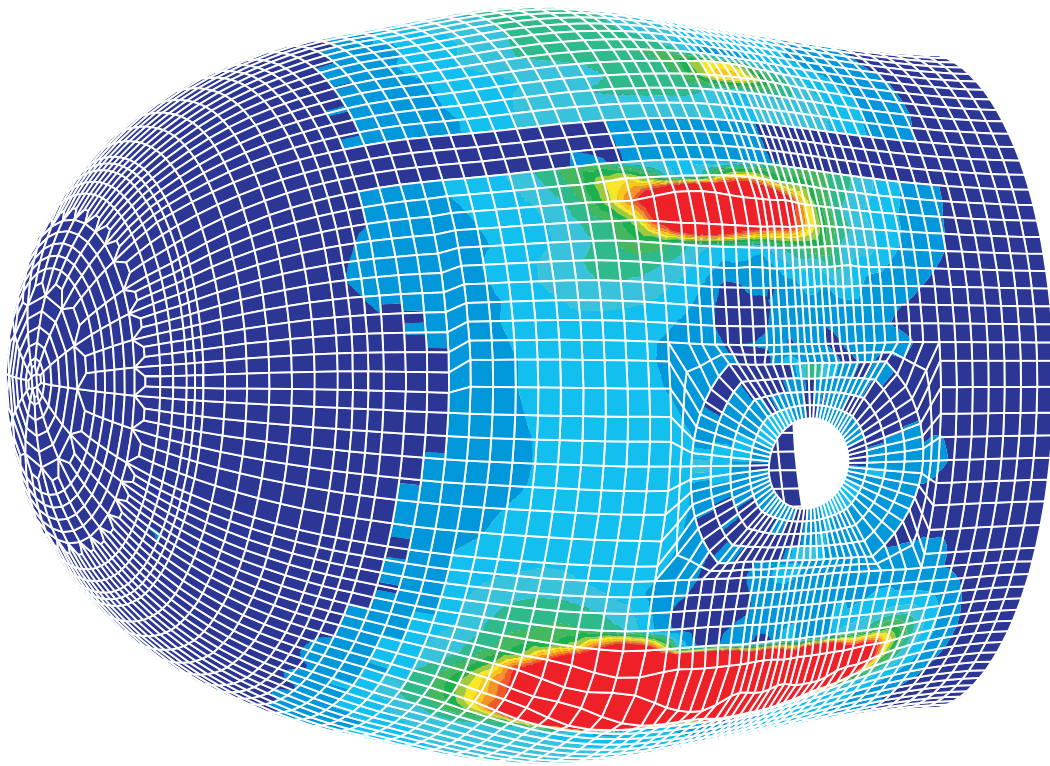


1.366 MPa

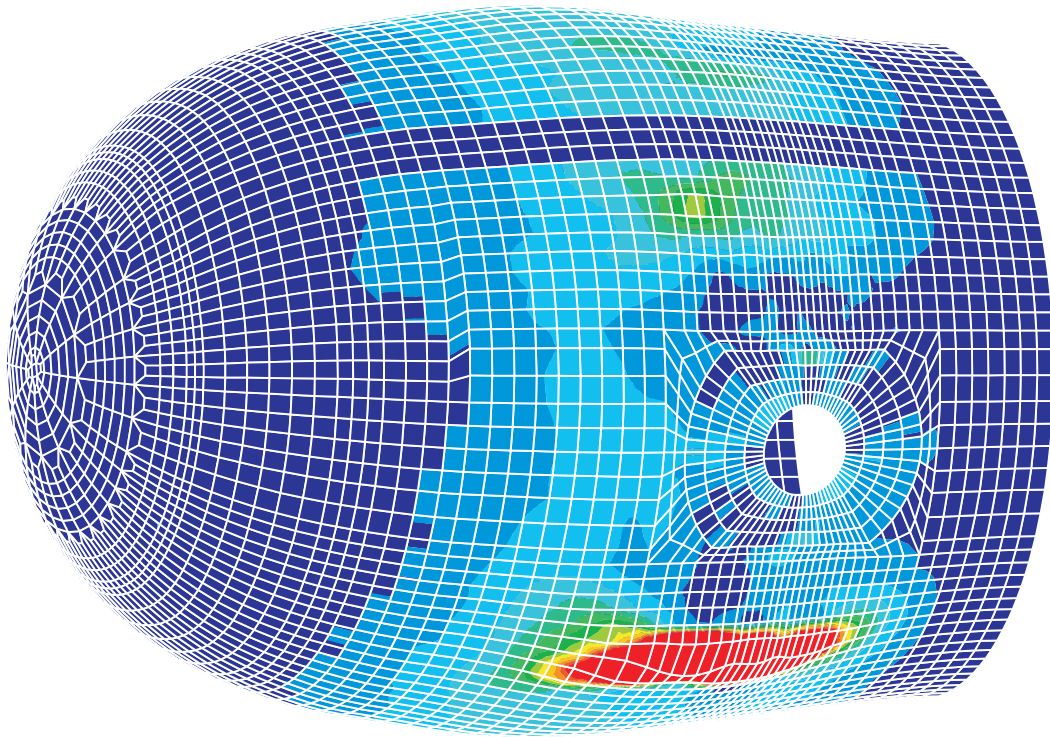


1.373 MPa

Figure 9-24. PCCV SFMT, 3D Global Shell Tendon Rupture Model. Concrete Maximum Principal Strain. For Pressure at 1.366 MPa (3.47 Pd) and 1.373 MPa (3.49 Pd), Displacement  $\times 10$ .



1.389 MPa



1.381 MPa

Figure 9-25. PCCV SFMT, 3D Global Shell Tendon Rupture Model. Concrete Maximum Principal Strain. For Pressure at 1.381 MPa (3.51 Pd) and 1.389 MPa (3.53 Pd), Displacement  $\times 10$ .

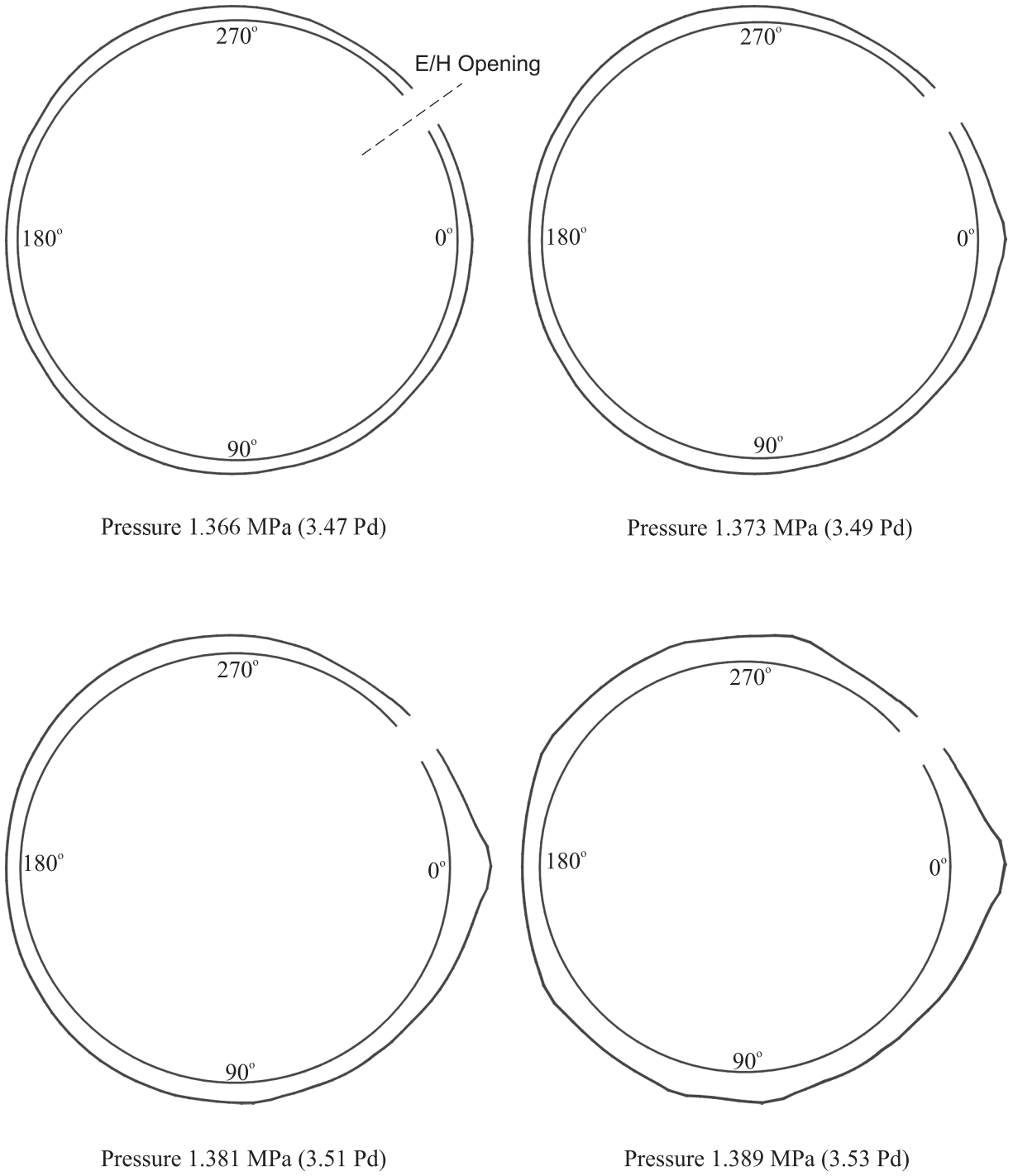
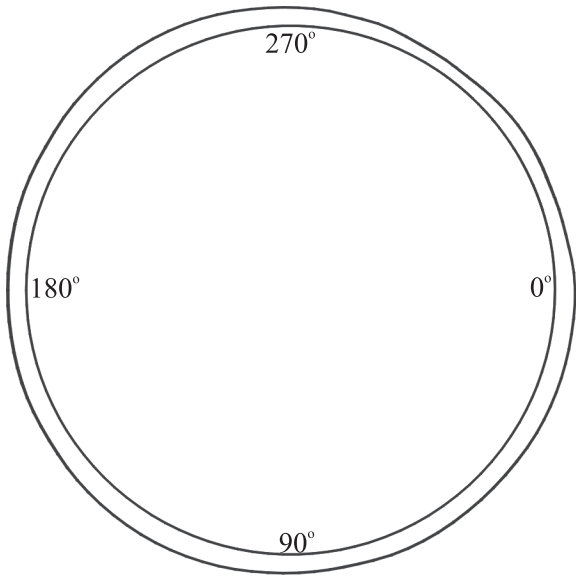
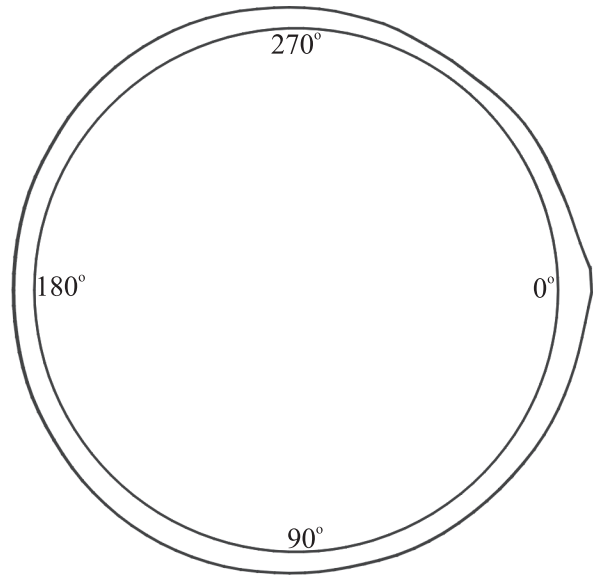


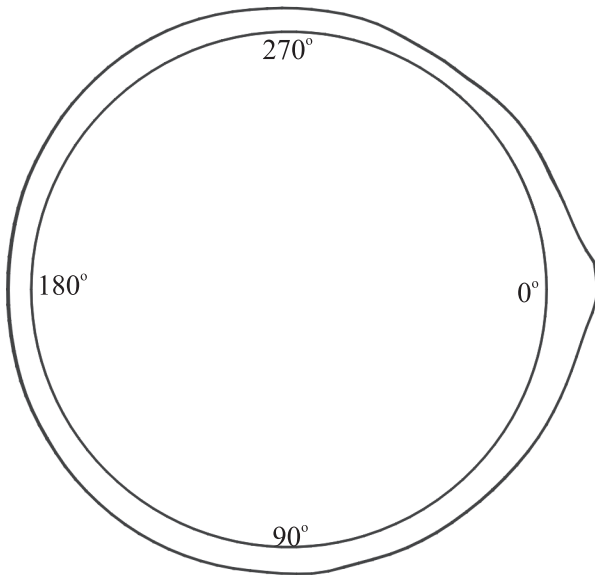
Figure 9-26. PCCV SFMT, 3D Global Shell Tendon Rupture Model.  
Deformed Shape. For Elevation of 5.4 m. Displacements  $\times 10$ .



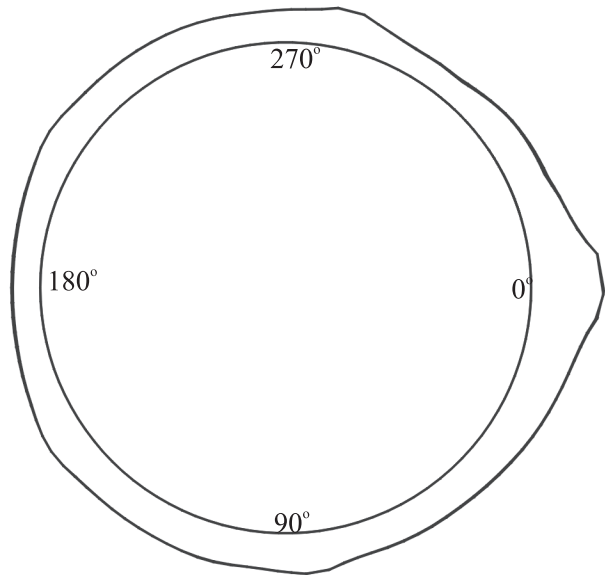
Pressure 1.366 MPa (3.47 Pd)



Pressure 1.373 MPa (3.49 Pd)



Pressure 1.381 MPa (3.51 Pd)



Pressure 1.389 MPa (3.53 Pd)

Figure 9-27. PCCV SFMT, 3D Global Shell Tendon Rupture Model.  
Deformed Shape. For Elevation of 6.5 m. Displacements  $\times 10$ .

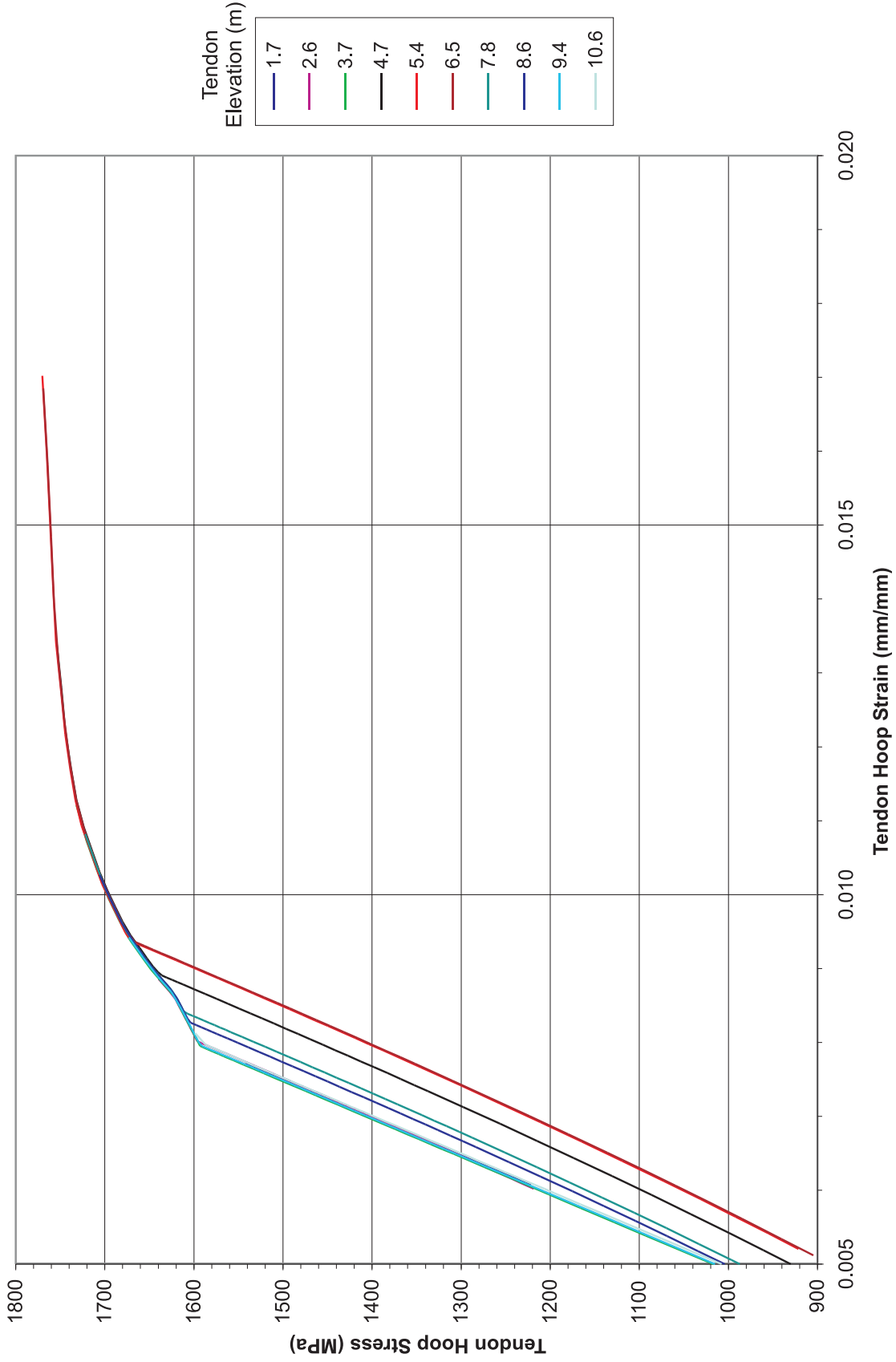


Figure 9-28. PCCV SFMT, 3D Global Shell Model-Hoop Tendon Stress Versus Strain History, Tendon History at 0 Degrees Azimuth, P = 1.357 MPa, 3.45 Pd

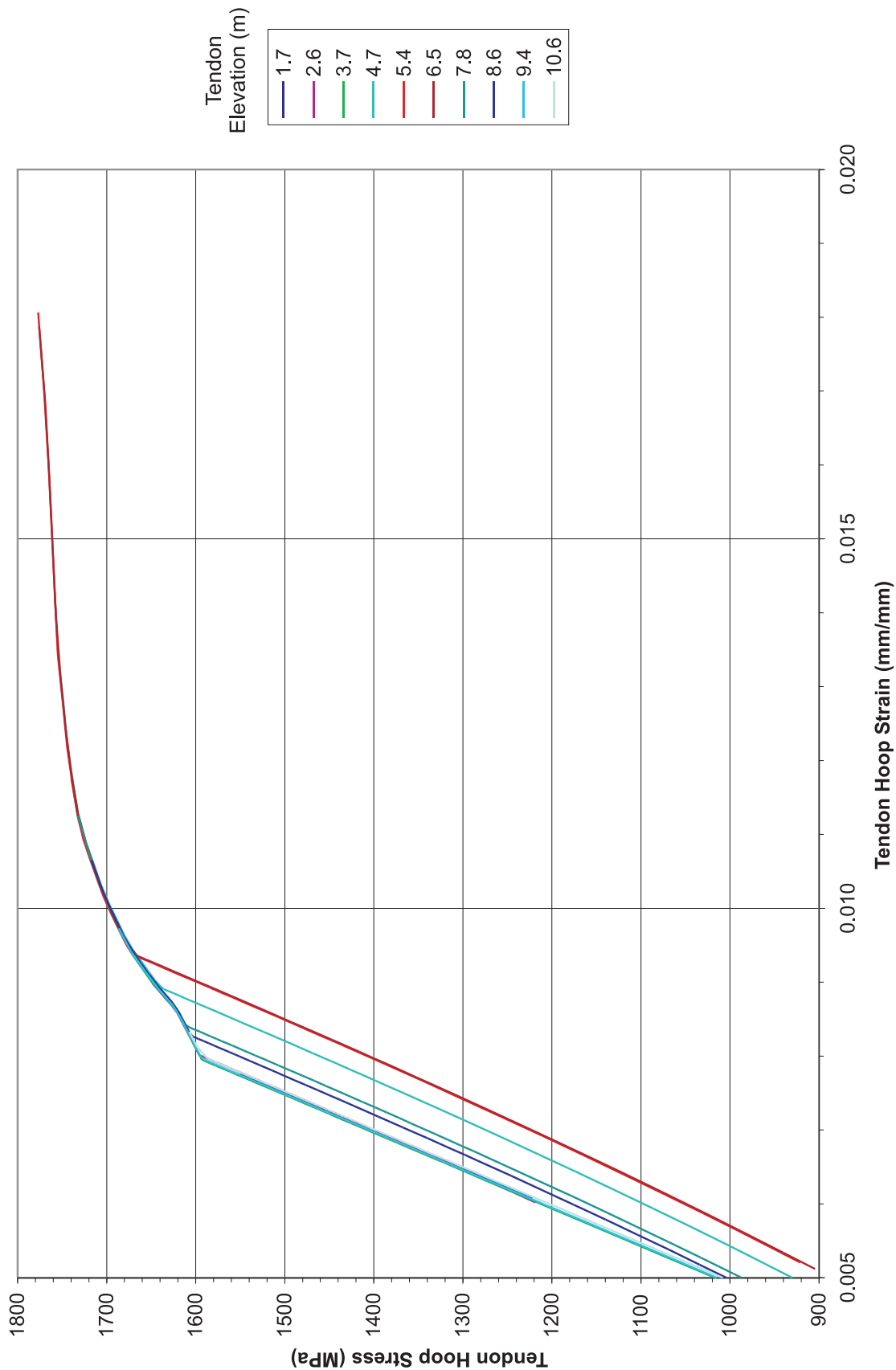


Figure 9-29. PCCV SFMT, 3D Global Shell Model-Hoop Tendon Stress Versus Strain History, Tendon History at 0 Degrees Azimuth, P = 1.366 MPa, 3.47Pd

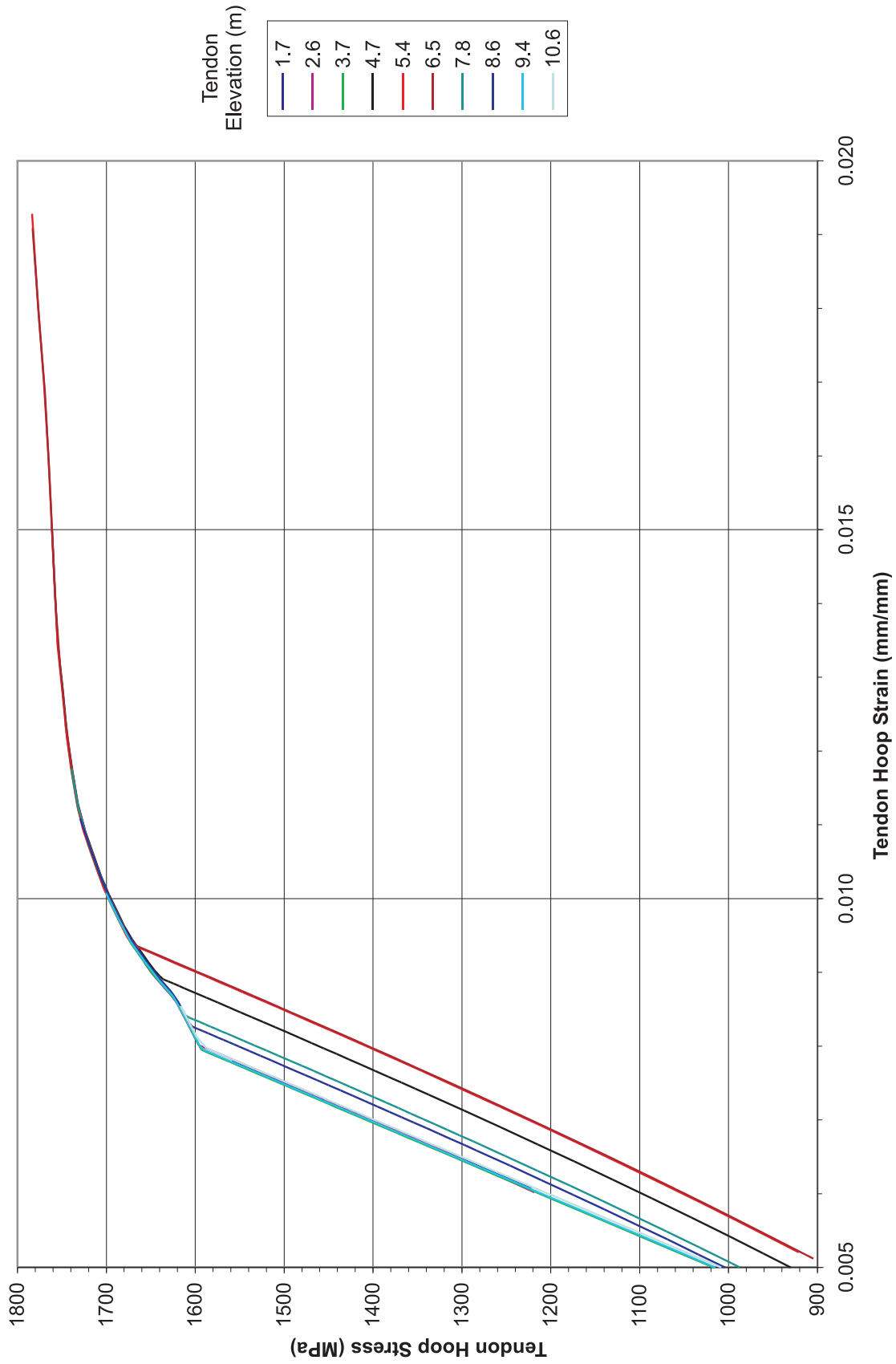


Figure 9-30. PCCV SFMT, 3D Global Shell Model-Hoop Tendon Stress Versus Strain History, Tendon History at 0 Degrees Azimuth, P = 1.373 MPa, 3.49 Pd

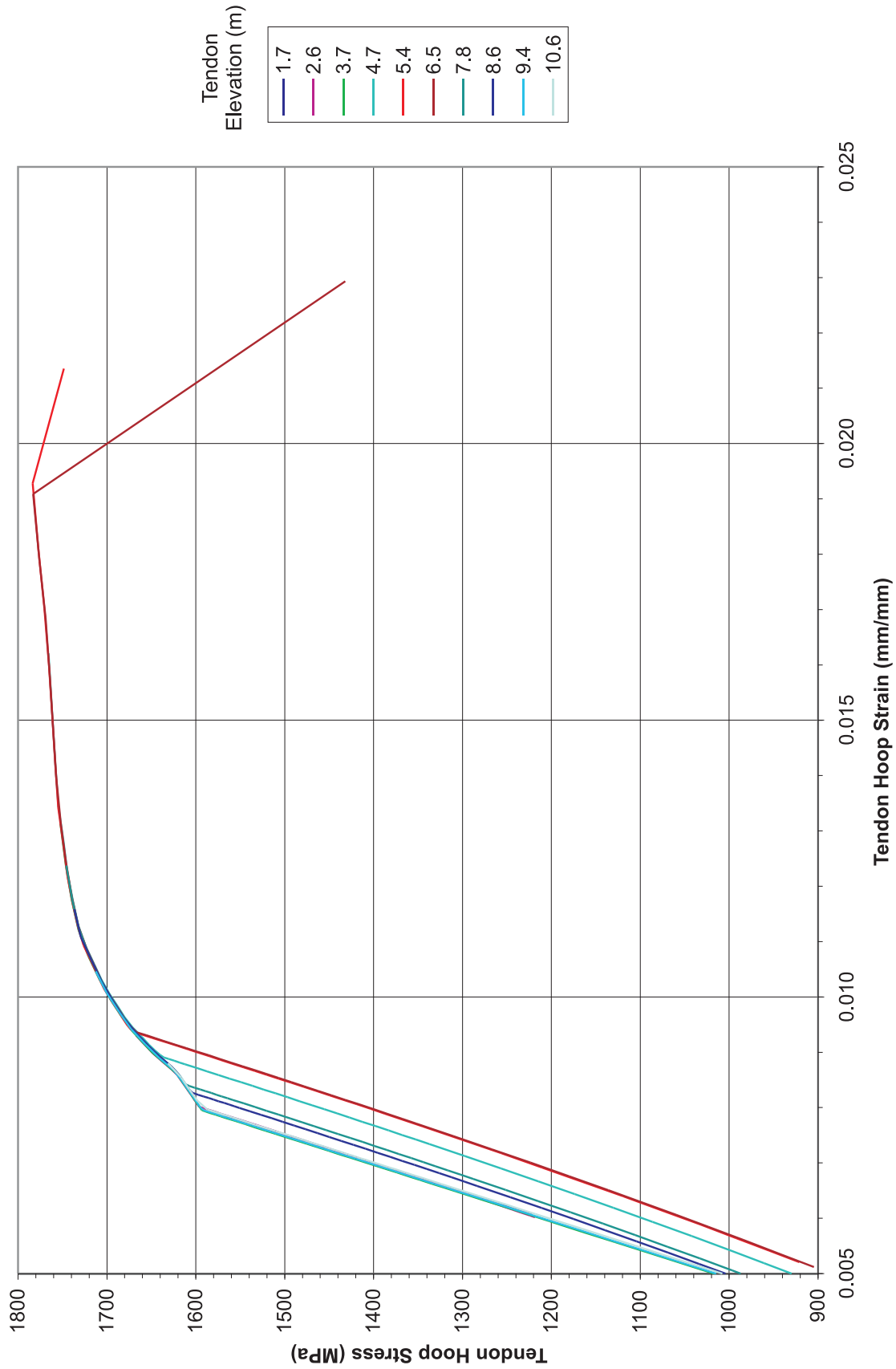


Figure 9-31. PCCV SFMT, 3D Global Shell Model-Hoop Tendon Stress Versus Strain History, Tendon History at 0 Degrees Azimuth, P = 1.381 MPa, 3.51 Pd

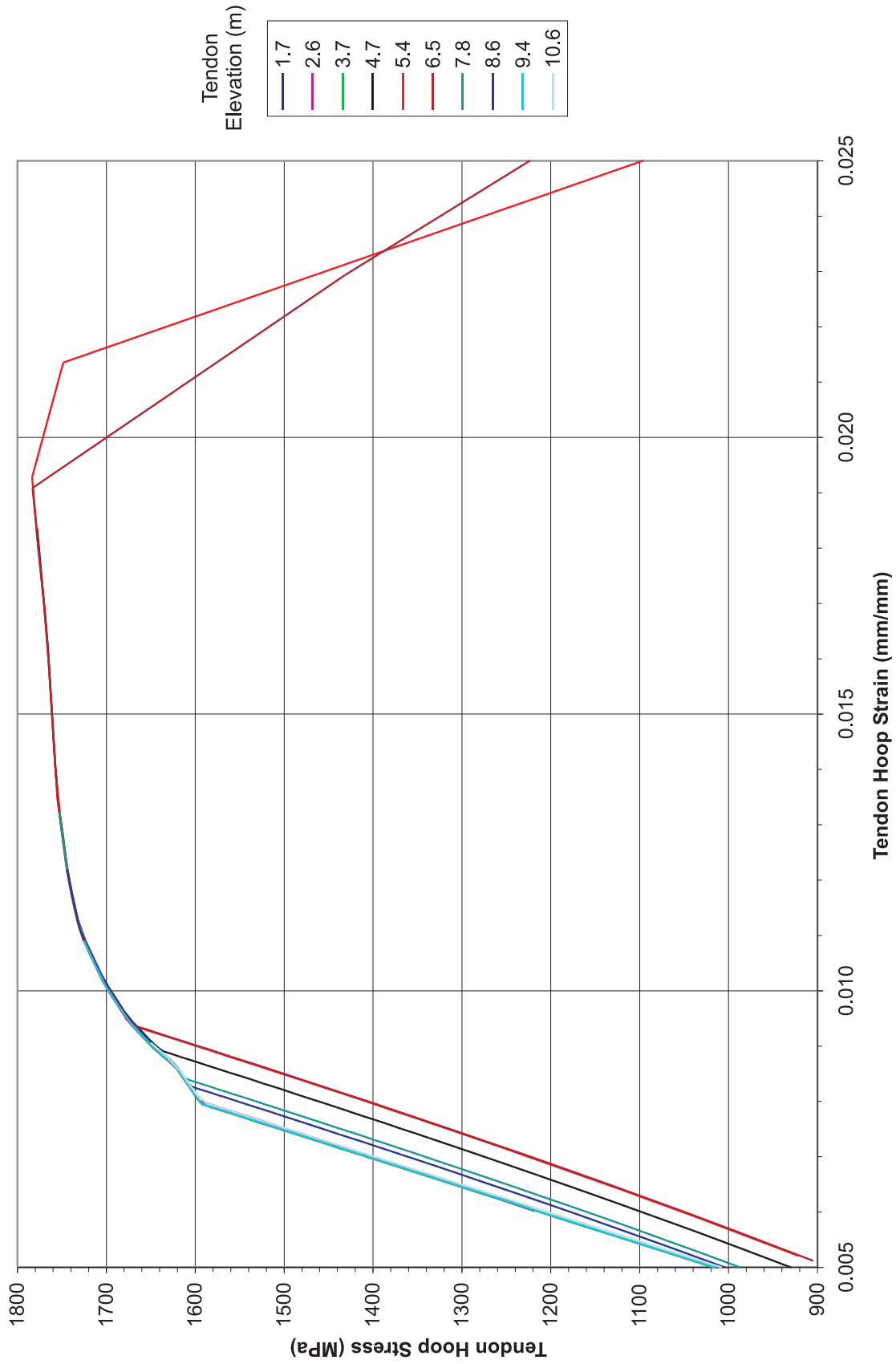


Figure 9-32. PCCV SFMT, 3D Global Shell Model-Hoop Tendon Stress Versus Strain History, Tendon History at 0 Degrees Azimuth, P = 1.389 MPa, 3.53 Pd

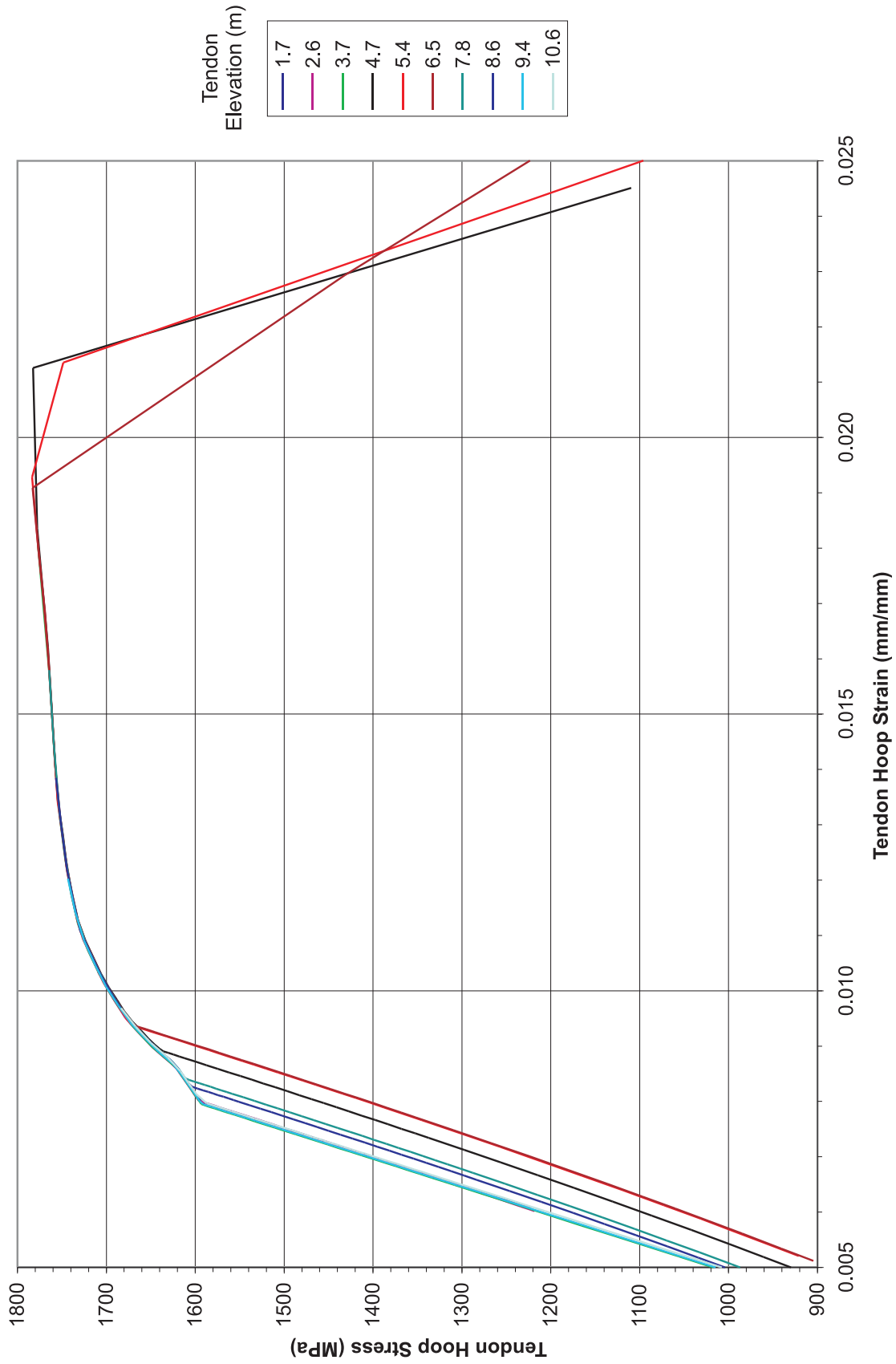


Figure 9-33. PCCV SFMT, 3D Global Shell Model-Hoop Tendon Stress Versus Strain History, Tendon History at 0 Degrees Azimuth, P = 1.404 MPa, 3.57 Pd

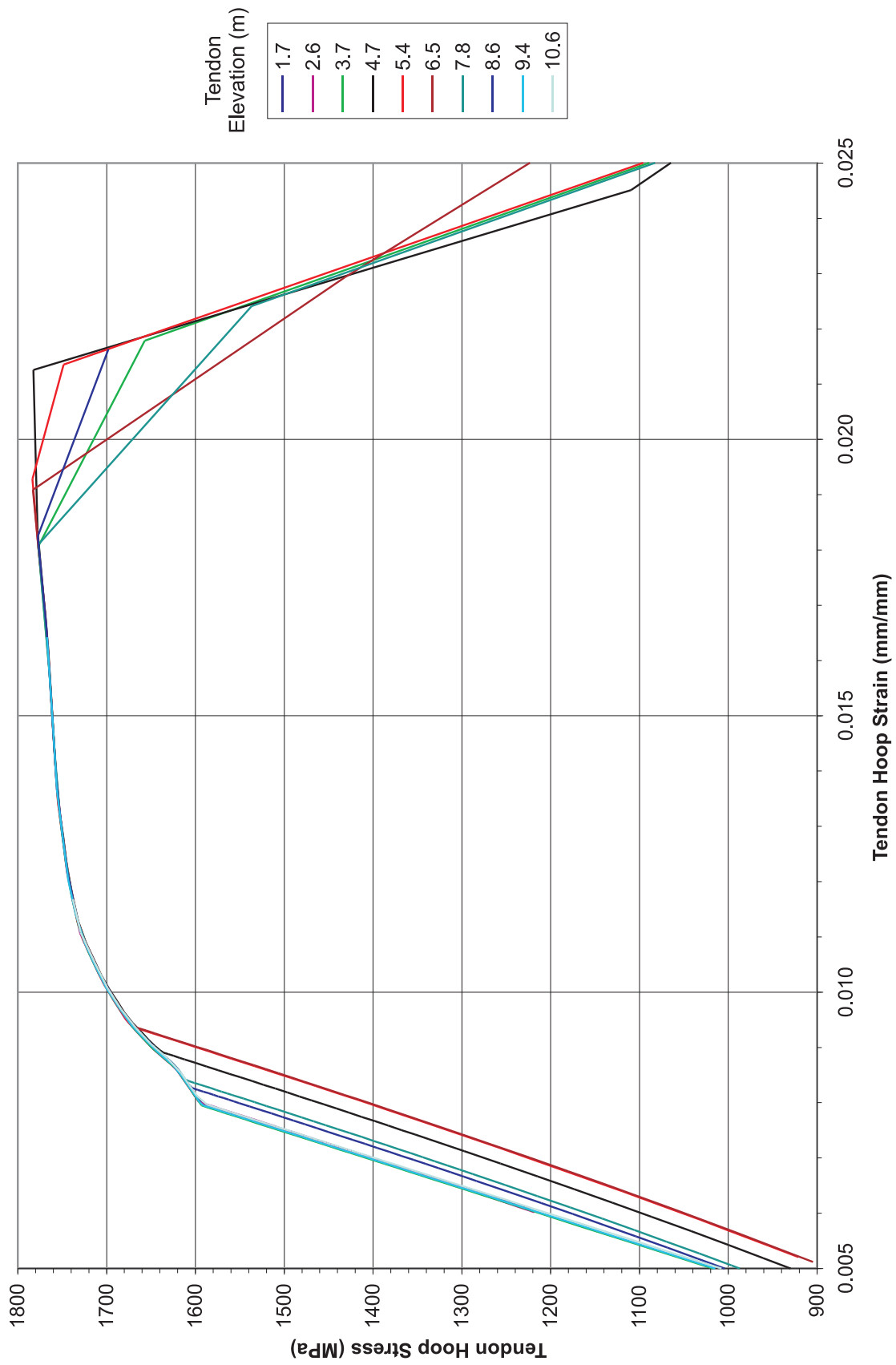


Figure 9-34. PCCV SFMT, 3D Global Shell Model-Hoop Tendon Stress Versus Strain History, Tendon History at 0 Degrees Azimuth, P = 1.436 MPa, 3.65 Pd

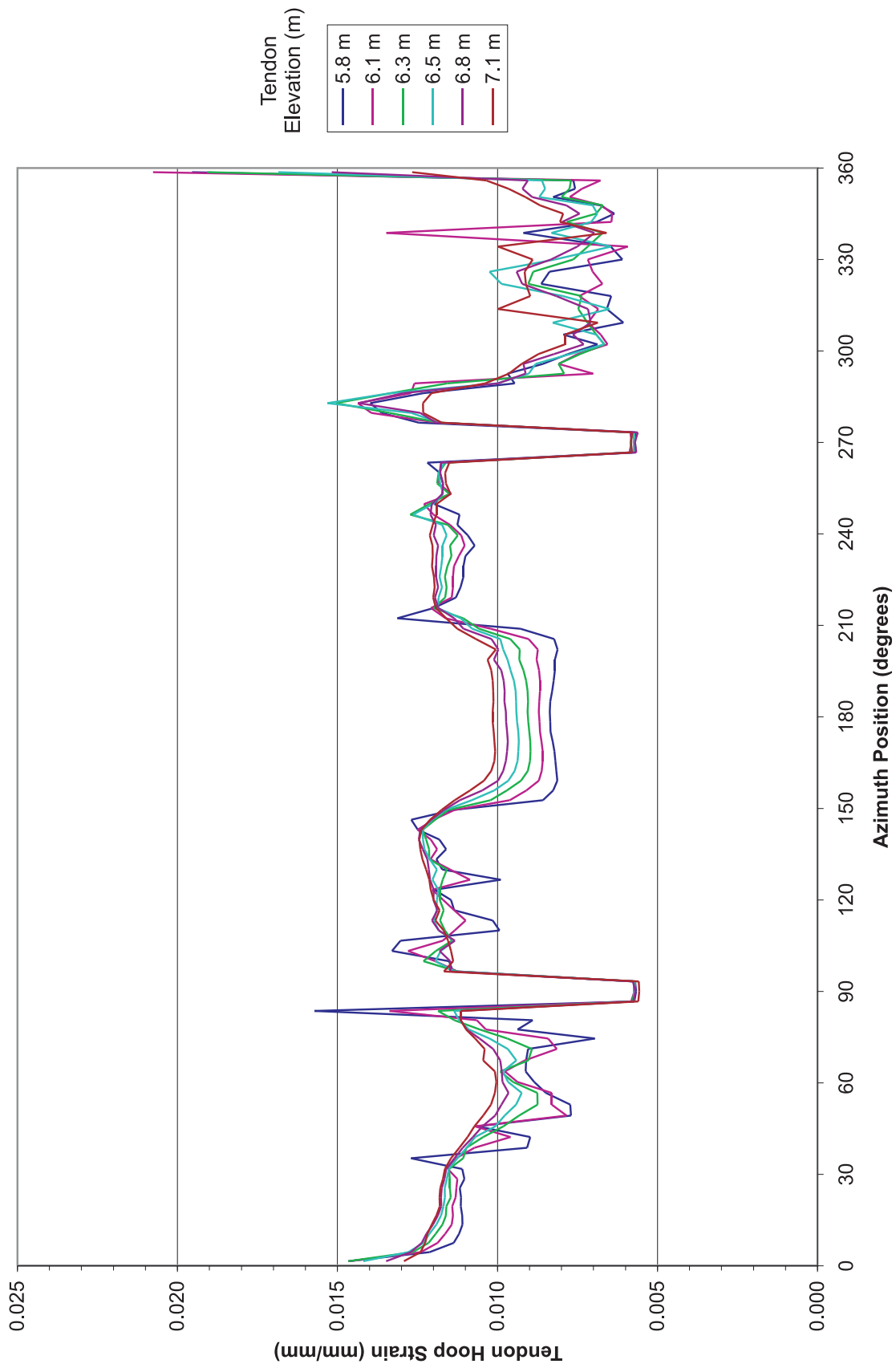


Figure 9-35. PCCV SFMT, 3D Global Shell Model-Hoop Tendon Strain Profile, Tendon History, P = 1.357 MPa, 3.45 Pd

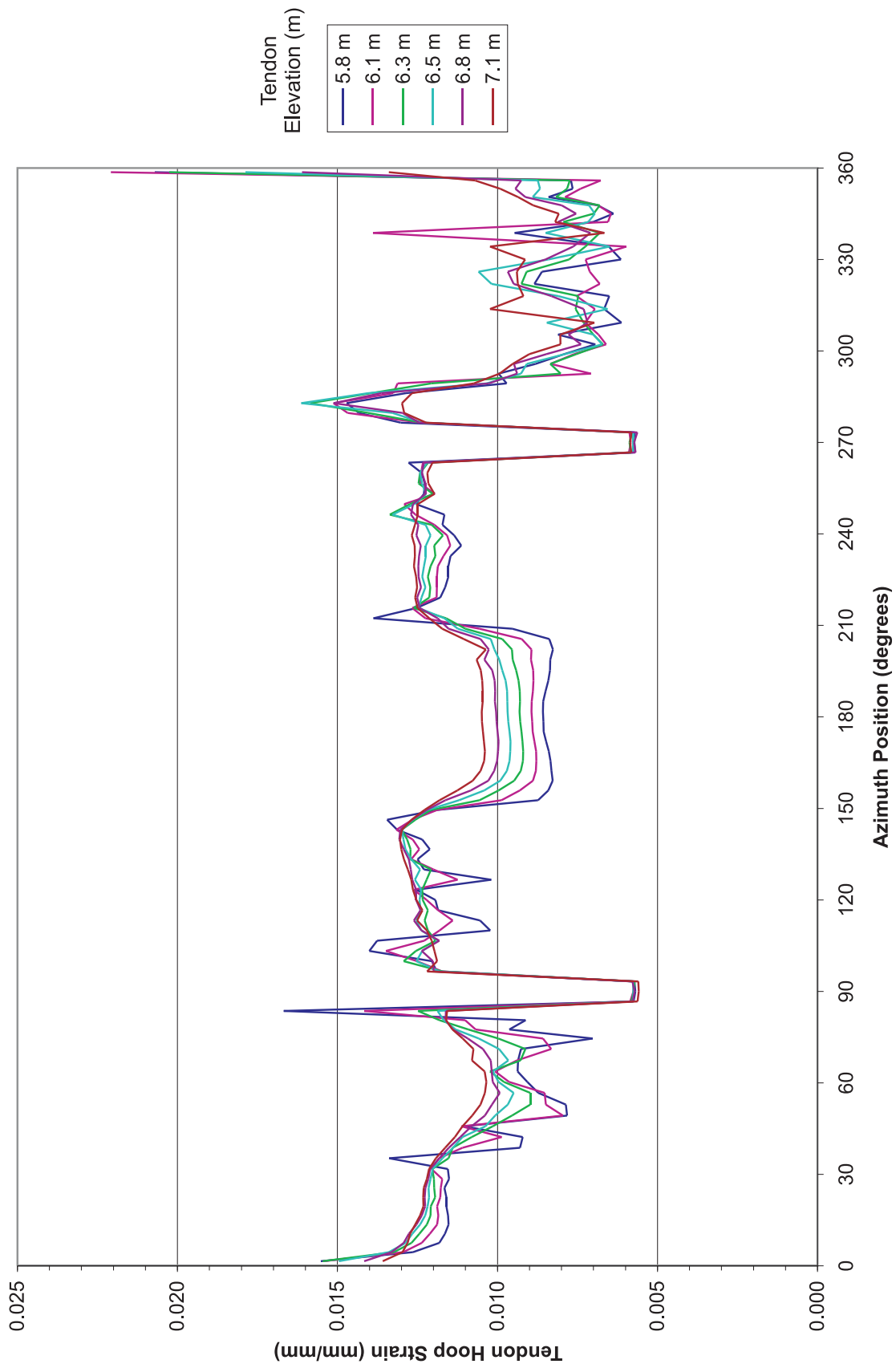


Figure 9-36. PCCV SFMT, 3D Global Shell Model-Hoop Tendon Strain Profile, Tendon History, P = 1.366 MPa, 3.47 Pd

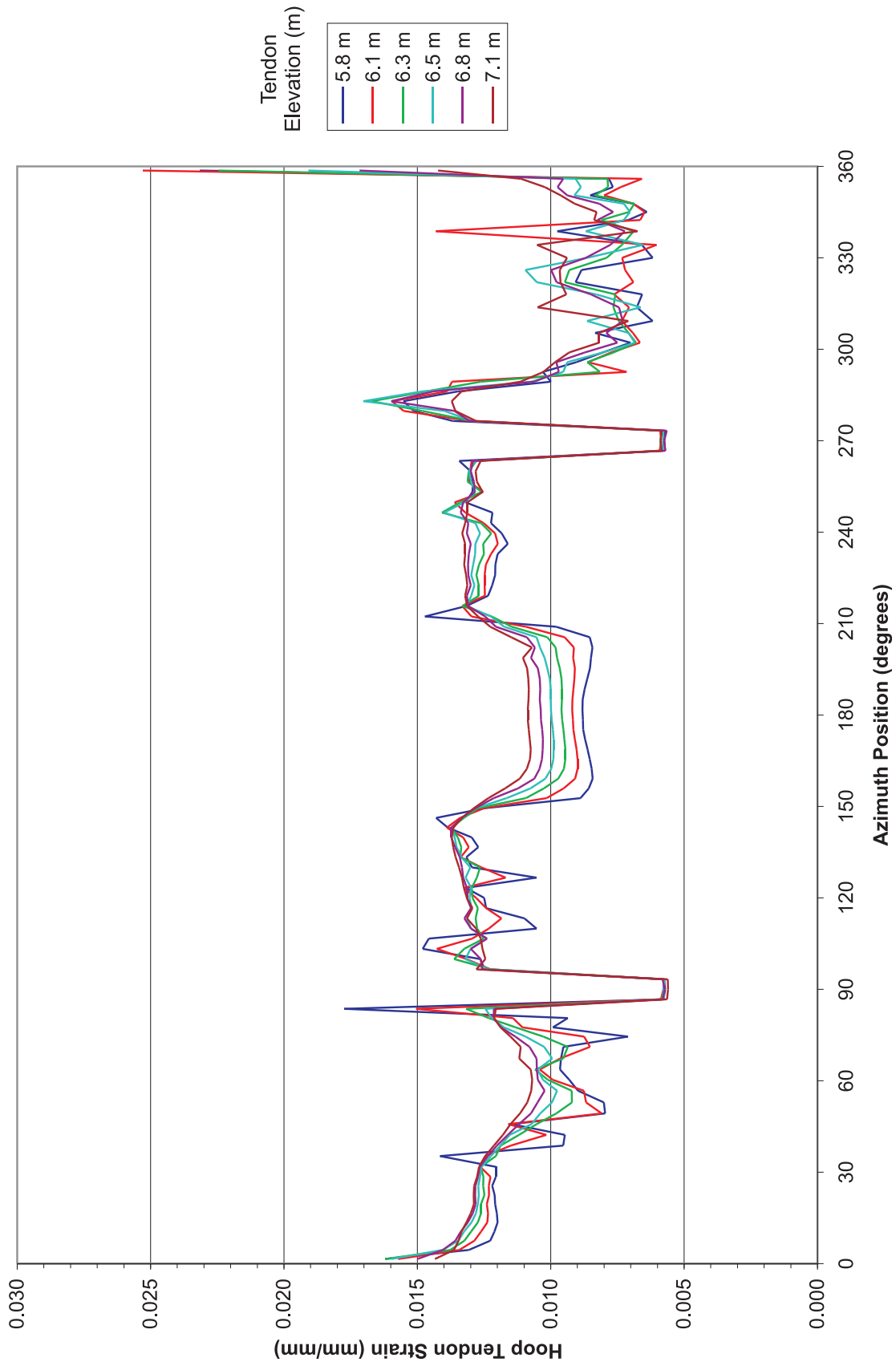


Figure 9-37. PCCV SFMT, 3D Global Shell Model-Hoop Tendon Strain Profile, Tendon History, P = 1.373 MPa, 3.49 Pd

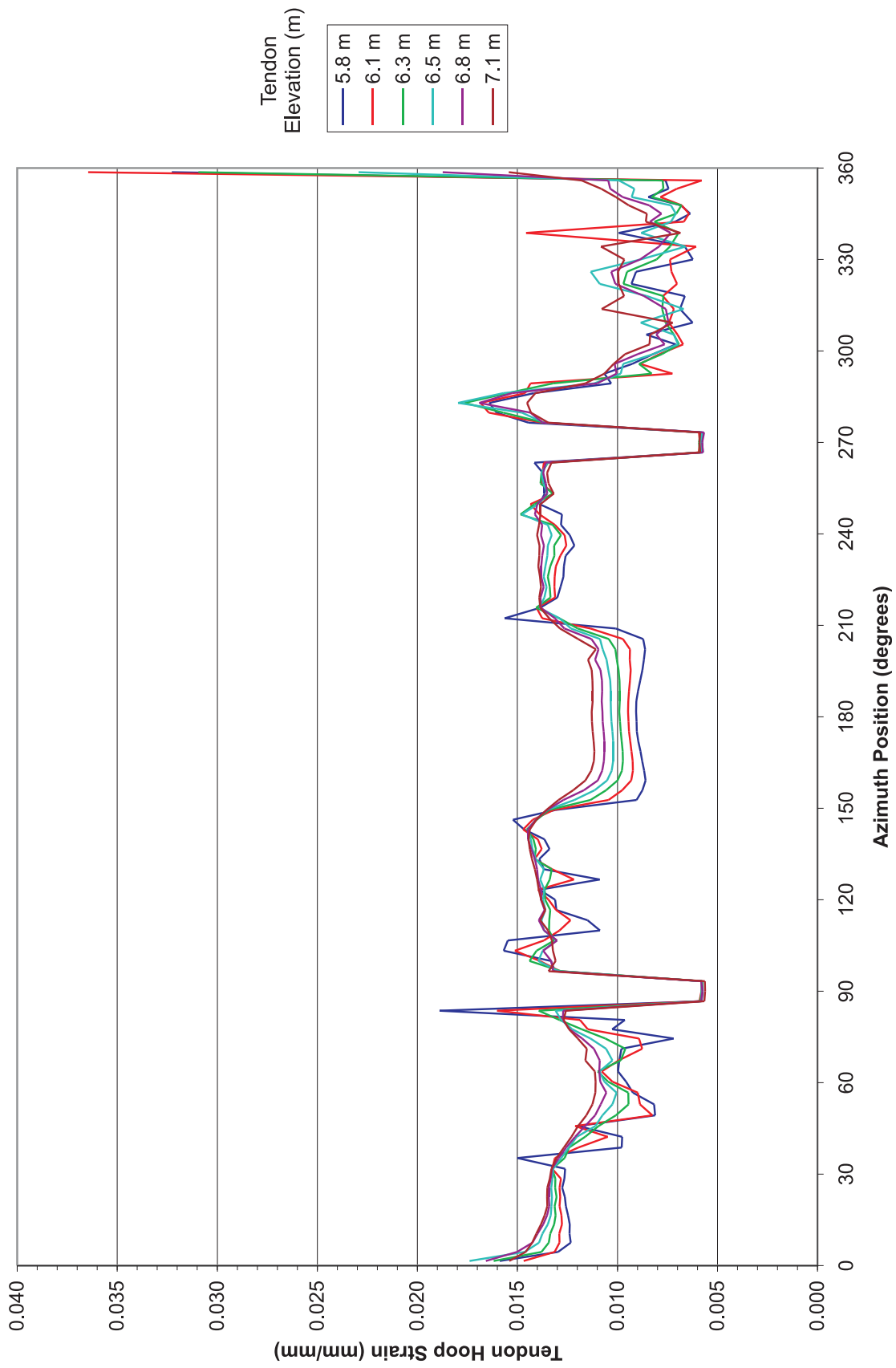


Figure 9-38. PCCV SFMT, 3D Global Shell Model-Hoop Tendon Strain Profile, Tendon History, P = 1.381 MPa, 3.51 Pd

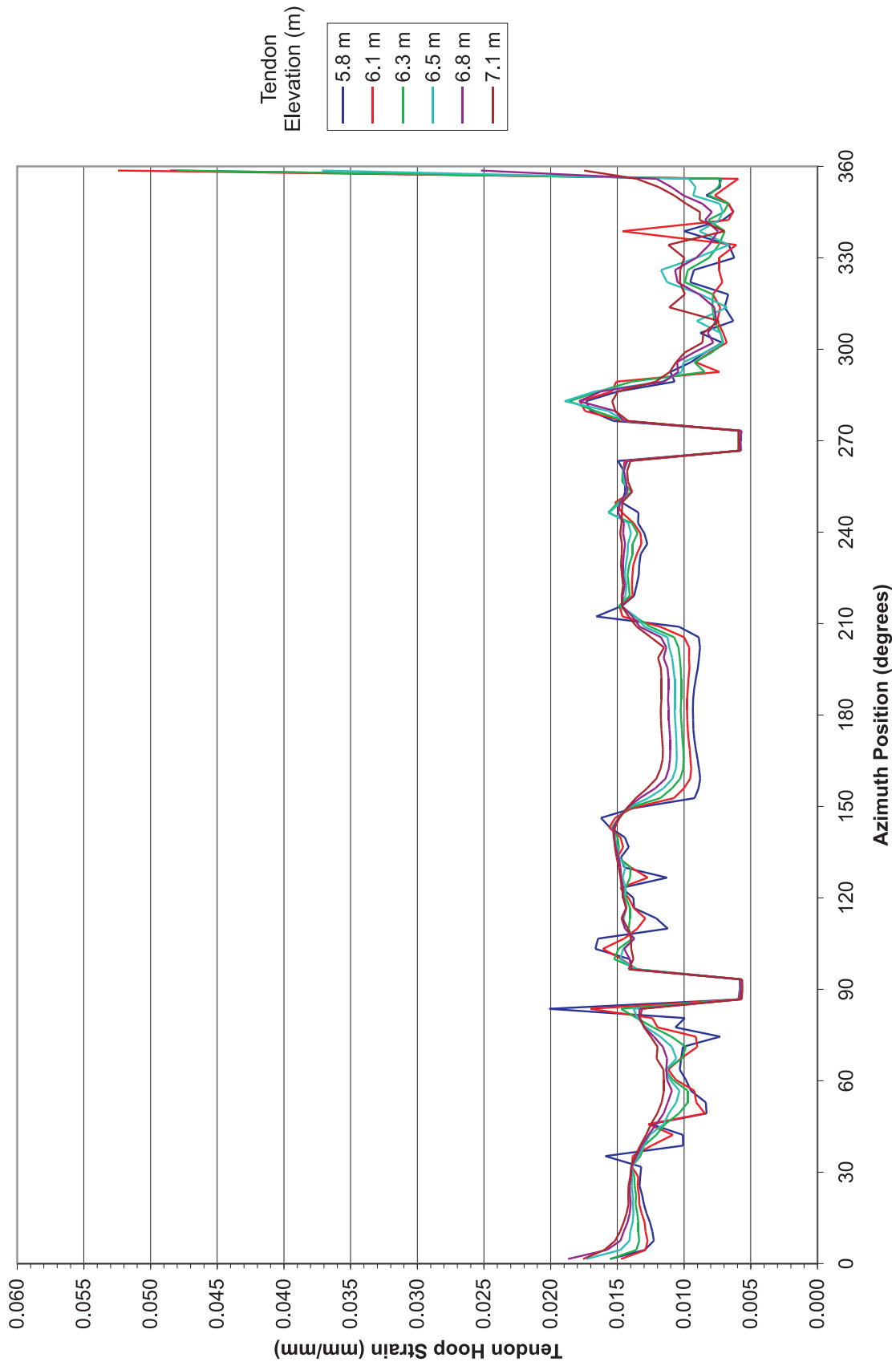


Figure 9-39. PCCV SFMT, 3D Global Shell Model-Hoop Tendon Strain Profile, Tendon History, P = 1.389 MPa, 3.53 Pd

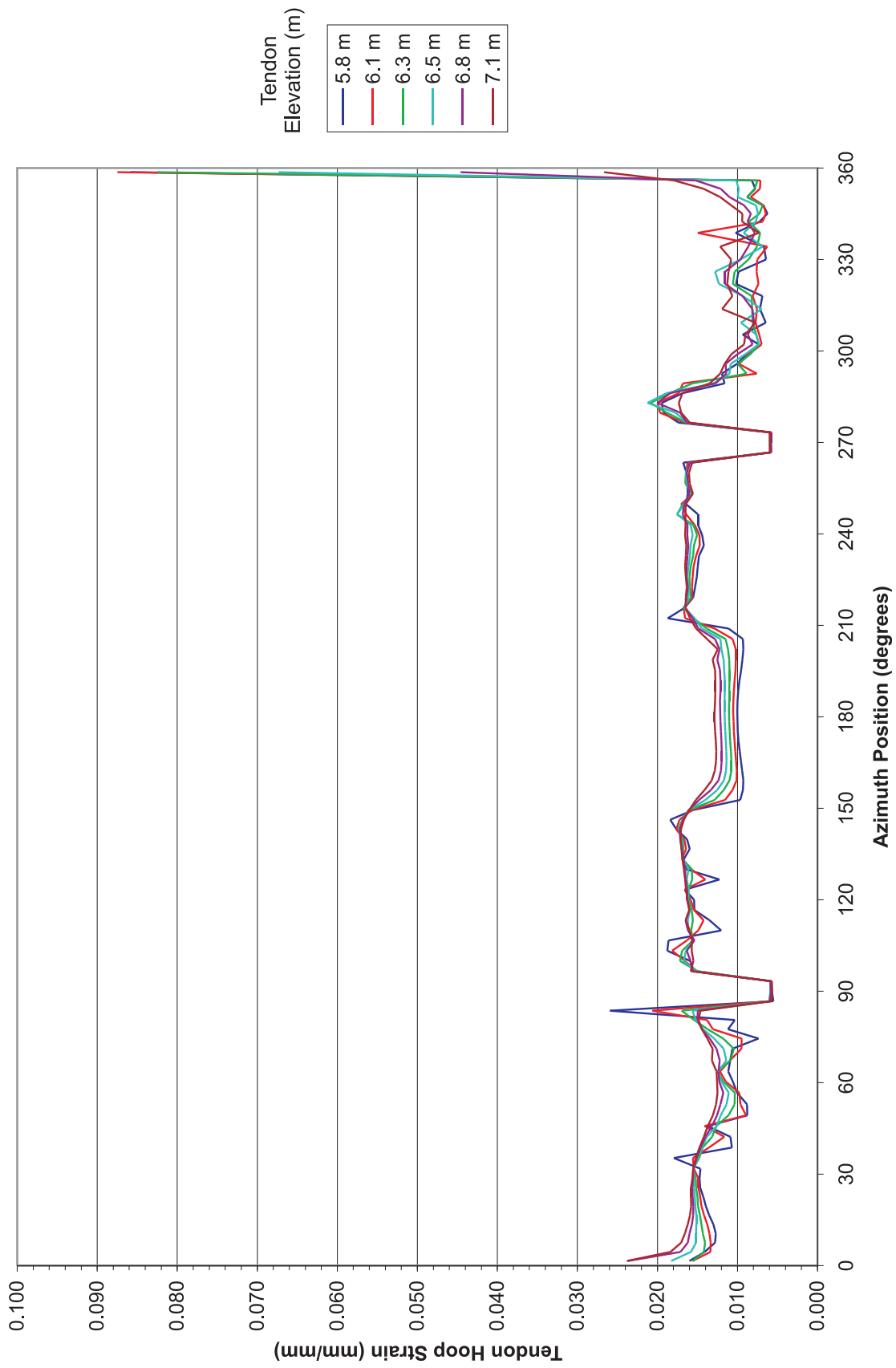


Figure 9-40. PCCV SFMT, 3D Global Shell Model-Hoop Tendon Strain Profile, Tendon History, P = 1.404 MPa, 3.57 Pd

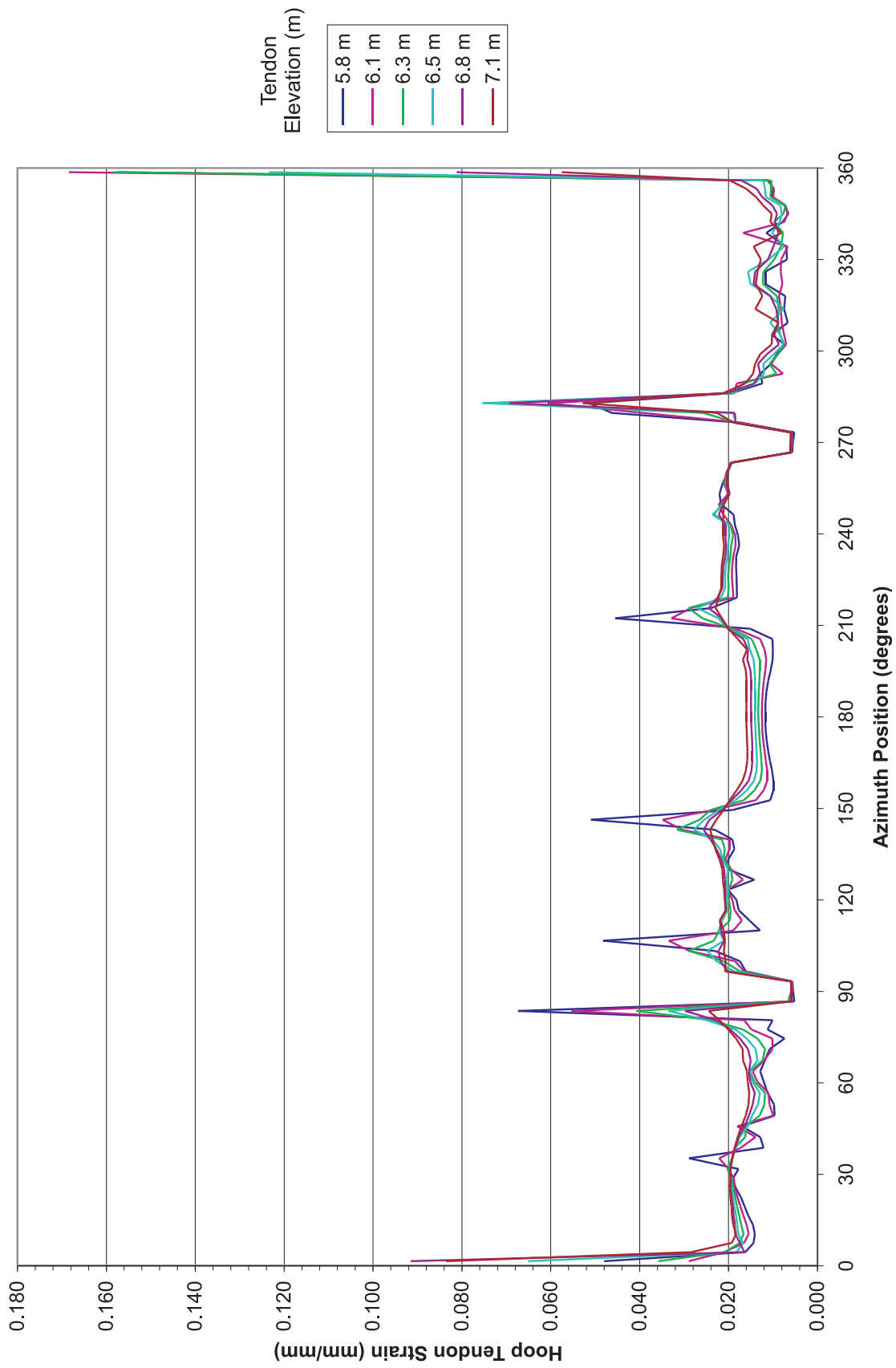


Figure 9-41. PCCV SFMT, 3D Global Shell Model-Hoop Tendon Strain Profile, Tendon History, P = 1.436 MPa, 3.65 Pd

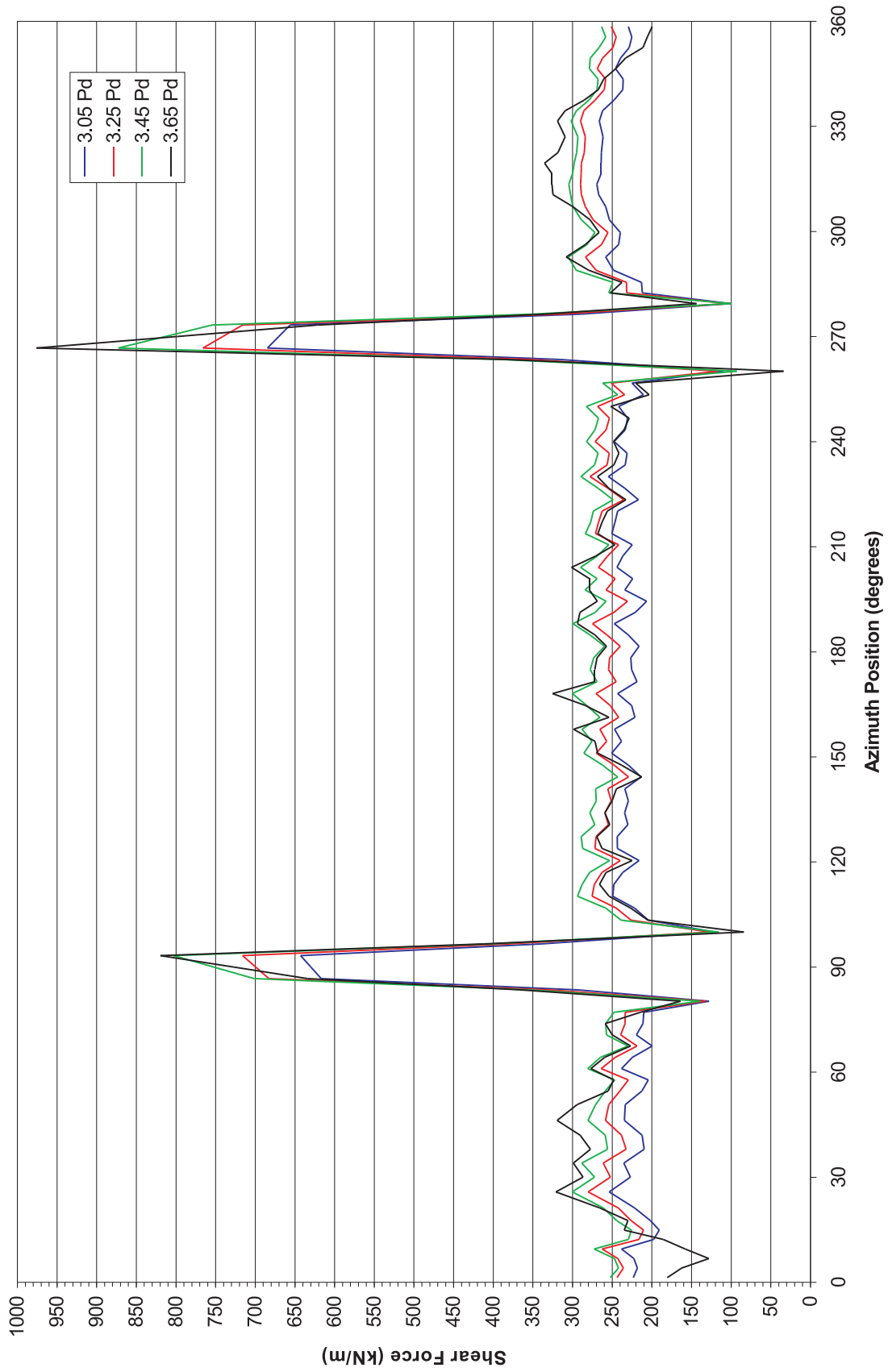


Figure 9-42. PCCV SFMT, 3D Global Shell Model - Cylinder Shear Profile 1 m Above Basemat

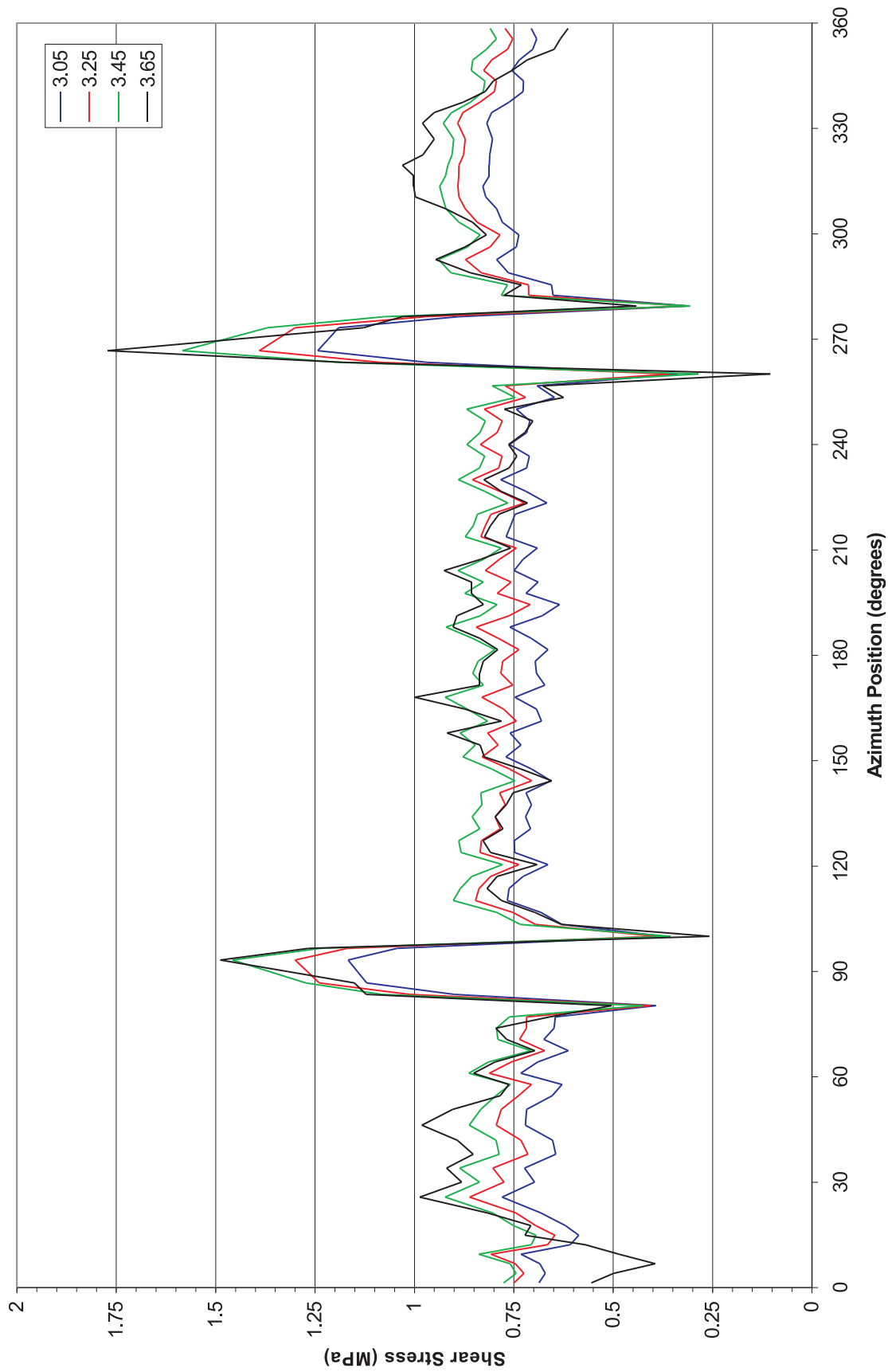


Figure 9-43. PCCV SFMT, 3D Global Shell Model - Cylinder Shear Profile 1 m Above Basemat

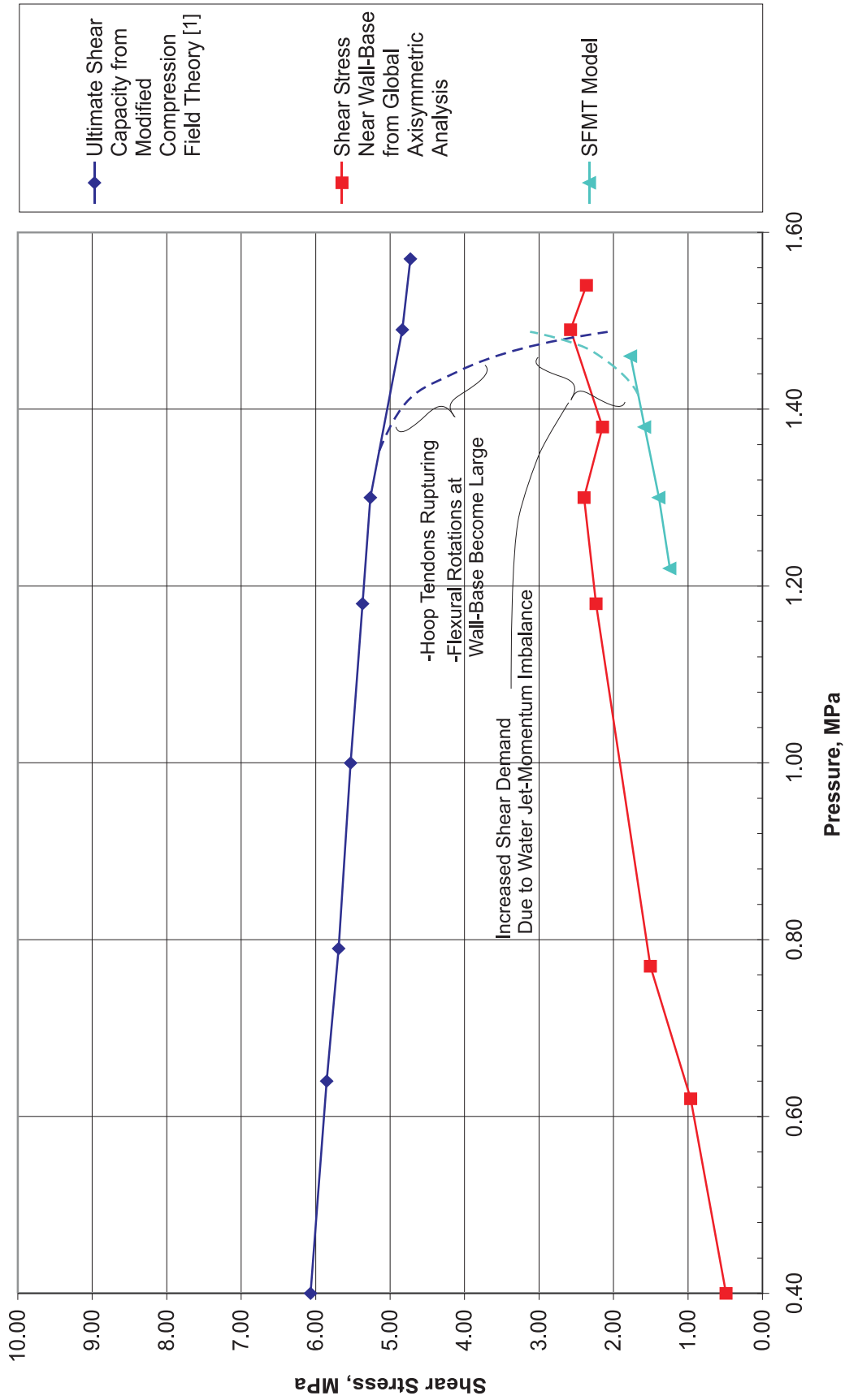


Figure 9-44. PCCV Wall-Base Shear Strength from Modified Compression Field Theory Compared to Shear Demand from the Global Analysis Model [1] and the SFMT Model

